
Article:
Ng, F.S.L., Igneczi, A., Sole, A.J. et al. (2018) Response of surface topography to basal variability along glacial flowlines. Journal of Geophysical Research: Earth Surface, 123 (10). pp. 2319-2340. ISSN: 2169-9011

https://doi.org/10.1029/2017JF004555

Journal of Geophysical Research: Earth Surface

RESEARCH ARTICLE
10.1029/2017JF004555

Key Points:
- We present an extended mathematical theory of how ice flow transfers basal variations upward to form undulating surface topography, for nonuniform flow in two dimensions
- We formulate an integral transform method for calculating such transfer along flowlines
- Validation of the method on synthetic flowlines informs its application to flowlines on valley glaciers and ice sheets

Correspondence to:
F. S. L. Ng,
f.ng@sheffield.ac.uk

Citation:
Ng, F. S. L., Ignéczi, Á., Sole, A. J., & Livingstone, S. J. (2018). Response of surface topography to basal variability along glacial flowlines. *Journal of Geophysical Research: Earth Surface*, *123*. https://doi.org/10.1029/2017JF004555

Received 15 NOV 2017
Accepted 27 JUN 2018
Accepted article online 6 AUG 2018

Response of Surface Topography to Basal Variability Along Glacial Flowlines

Felix S. L. Ng[1], Ádám Ignéczi[1], Andrew J. Sole[1], and Stephen J. Livingstone[1]

[1]Department of Geography, University of Sheffield, Sheffield, UK

Abstract Predicting the amplitude and distribution of surface undulations on ice sheets and glaciers is useful because of their influence on surface mass and energy balance, atmospheric boundary layer processes, and supraglacial meltwater routing. We develop an approximate method of calculating the surface elevation response due to spatial perturbations in basal topography and slipperiness, on two-dimensional flow sections whose thickness, surface slope, and basal slip ratio vary along flow. Our main result is an integral expressing nonuniform transfer of basal variability to the surface. It uses published Fourier transfer functions derived through perturbing plane-slab Stokes flow but circumvents the need to subwindow the spatial domain to estimate the response. We test the method on ice flow synthesized by a finite-element model of Stokes flow with constant viscosity and known basal topography and slipperiness perturbations; in this case, it predicts the observed size and shape of the surface undulations well, capturing more than 90% of their variance. Application of the method to the central flowline of Columbia Glacier, Alaska, and a flowline on the Greenland Ice Sheet ending on Nordenskiöld Glacier, using knowledge of the approximate bed topography and ignoring the unknown slipperiness forcing, yields less faithful prediction of their surface undulations (40–50% of their variance) but demonstrates the method's potential to reproduce their qualitative features. We discuss the factors limiting the method's performance on real flowlines.

1. Introduction

Ice sheets and glaciers exhibit short length scale variations in surface elevation—or *undulations*—superimposed upon their shape. These undulations stem from diverse causes such as ice flow over a nonuniform bed (Budd, 1970; Gudmundsson, 2003), spatial variation in surface mass balance (Black & Budd, 1964; Gow & Rowland, 1965; Whillans, 1975), heterogeneous snow compaction rates (Medley et al., 2015), and unsteady glacier dynamics (e.g., surges; Murray et al., 1998). We focus on predicting those undulations due to the first cause, which are often pronounced at wavelengths of 10^{-1} to 10^{1} km—shorter than an ice mass's length/span, but longer than length scales where forms arising from surface processes (e.g., sastrugi) are abundant. These *mesoscale* undulations are important for setting the regional ice surface slopes and roughness that influence surface mass and energy balance and atmospheric boundary layer processes (Arnold et al., 2006). They also control supraglacial meltwater routing (Karlstrom & Yang, 2016); notably, closed surface depressions provide sites for lake formation (Ignéczi et al., 2016; Lampkin & VanderBerg, 2011). The potential for basal variability to induce surface undulations that in turn affect supraglacial drainage is pertinent for the Greenland Ice Sheet and mountain glaciers today, especially as changes in surface hydrology and its linkage to the bed (via moulins) can influence basal sliding (Joughin et al., 2013; Wyatt & Sharp, 2015).

Although one can predict the detailed surface topography by solving the incompressible Stokes equations of ice flow at fine resolution, doing so is computationally expensive in long-time simulations of large-scale glacier/ice sheet behavior. It is more efficient to capture the topography and motion with a coarse numerical grid and fill in the details by computing the undulations. We develop a way of doing so in this paper.

Our method draws on existing analyses that perturb steady laminar flow on an inclined bed to find the surface elevation response to small-amplitude basal forcings. A key idea here is that ice flow acts as a filter for upward transmission of basal variability. Gudmundsson (2003; abbreviated *G2003* herein) developed a comprehensive theory of this by extending previous work (Jóhannesson, 1992; Reeh, 1987) and considering variability in basal topography (e.g., bumps) and basal slipperiness (e.g., sticky/slippery spots). His analysis uses the Stokes equations as the starting point and fully accounts for longitudinal stress effects. G2003 predicts efficient transfer of basal topographic variations whose wavelengths are a few times to tens of times of the ice thickness when ice flow occurs at high slip ratio (basal sliding velocity divided by ice deformational

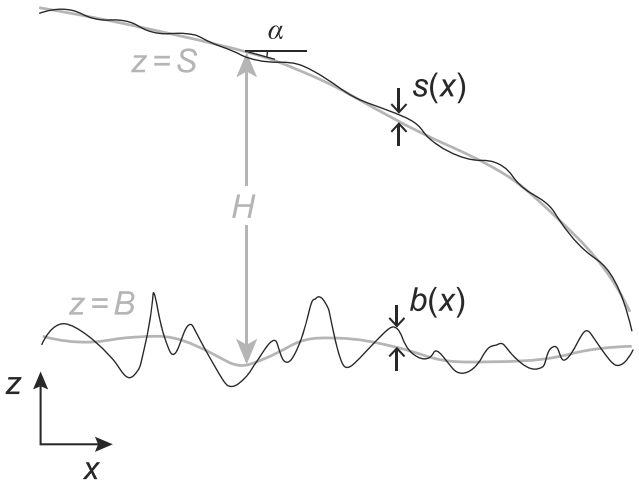

Figure 1. Schematic of flowline cross section and topographical symbols.

velocity). This prediction accords with the abundance of surface undulations on active ice streams, as has been verified using their topography and flow speed (De Rydt et al., 2013).

G2003 assumed a plane-parallel slab flow with constant viscosity as the background state for imposing perturbations. The resulting linearized problem admits Fourier transform solutions; the transmission is described by Fourier domain transfer functions, whose product with the Fourier transforms of the basal variability gives the Fourier transform of the surface undulations. De Rydt et al. (2013) tested this theory on ice stream trunks where the parallel approximation holds. However, it is unknown how the theory can be used where this idealization fails—namely, on *nonuniform* glacier/ice sheet flowlines along which ice thickness and velocity vary considerably. Here we describe an approximate method of calculating the corresponding surface response due to basal variability, using the same transfer functions derived for constant viscosity. It opens the way for more comprehensive application of G2003's theory. To keep the exposition simple, we focus on two-dimensional (2-D) steady plane flow. Our emphasis is on initial development of the method and demonstration of its feasibility through a few synthetic and real case studies. While we discuss its limitations, deriving analytical error bounds and testing on many flowlines to understand the precise factors governing its accuracy are beyond our current scope. Exploration of the subject is thus by no means complete.

2. Mathematical Theory

Consider a vertical glacial flowline section (Figure 1). Let x be horizontal distance along flow and z be the vertical coordinate. We denote the smooth (*background*) profiles of surface and bed elevation by $S(x)$ and $B(x)$, respectively, and short-scale perturbations (*variability*) upon these by $s(x)$ and $b(x)$—in lowercase, so the true elevations are $S + s$ and $B + b$. By mesoscale, we mean perturbations with wavelengths of about 1 (or a fraction of one) to 10 times (or several tens) ice thickness. We denote the basal slipperiness perturbation by $c(x)$, following G2003's definition that c measures normalized (dimensionless) deviations of the sliding parameter C in the basal sliding law: that is, $u_b = C(1 + c)\tau_b$, where u_b is sliding speed and τ_b is basal shear stress. Thus, $C(x)$ and $c(x)$ respectively represent background and variability contributions to sliding. The basal slip ratio is defined as

$$\gamma = \frac{u_s}{u_d} - 1, \tag{1}$$

where u_s and u_d are background profiles of surface flow speed and ice deformation speed, respectively. The $\gamma(x)$ is a background control in the transfer functions of G2003.

The decompositions above assume a reasonable *separation of length scales* between background variations and perturbations. Formally, this would allow the Stokes flow problem to be expressed as a multiple-scale asymptotic expansion (e.g., Kevorkian & Cole, 1996), which uses the small ratio of the two length scales—called the *scale-separation parameter*—to construct approximations to the flow solution. In such framework, which motivates our method, perturbation analysis can in principle be performed on any nonuniform background (steady) flow state to link response $s(x)$ to the basal variability. The linearized flow problem is then inhomogeneous. One could seek its Green's function—the position-dependent impulse response—and use this to implement the transmission, but this avenue is difficult and not pursued here. Instead, we formulate an approximate method using G2003's transfer functions, by assuming that they approximate the effect of the Green's function when the background variables (e.g., ice thickness and slip ratio) change slowly along the flowline, which is a condition compatible with scale separation. The approximation arises because the linearized problem becomes homogeneous (has constant coefficients representing parallel-slab flow) when background variations vanish. The resulting approach circumvents the difficulty of calculating the multiple-scale expansion to the first-order approximation (which is needed when the scale-separation parameter is numerically nonnegligible). As the bed-to-surface transmission varies spatially, the transfer functions

cannot be applied multiplicatively on the Fourier transforms of the forcings; hence, our challenge is to calculate *nonuniform* transfer/filtering. (For terminology related to equation (6), we also refer to *nonstationary* transfer, but strictly in the spatial sense.) We derive our method in section 2.2 after introducing the transfer functions.

2.1. Fourier Domain Transfer Functions

For parallel slab flow with constant viscosity and thickness H (= $S(x) - B(x)$), surface slope angle α, and slip ratio γ (all these being constants), G2003 derived the following transfer functions describing the long-time ($t \to \infty$) spectral response of the surface due to the two kinds of basal variability:

$$T_{\mathrm{sb}}(\kappa) = \frac{[(1+\gamma)P + (1+\gamma+\kappa^2\gamma^2)\cosh\kappa]\kappa^2}{\kappa^2(1+\gamma)[1+\kappa^2(1+\gamma)+P\cosh\kappa] - i\cot\alpha(P\sinh\kappa - \kappa)}, \tag{2}$$

$$T_{\mathrm{sc}}(\kappa) = \frac{-\kappa^2\gamma\cosh\kappa}{\kappa^2(1+\gamma)[1+\kappa^2(1+\gamma)+P\cosh\kappa] - i\cot\alpha(P\sinh\kappa - \kappa)} \tag{3}$$

(equations (72) to (75) of G2003). Here $P(\kappa) = \cosh\kappa + \kappa\gamma\sinh\kappa$, and the dimensionless wavenumber κ is scaled to H, that is, $\kappa = 2\pi/(\lambda/H)$ if λ denotes horizontal wavelength, so the dimensional wavenumber is $k = \kappa/H$. The subscripts of T signify the transfer type: *sb* refers to variability in bed topography causing the surface response, and *sc* to variability in basal slipperiness causing the response. We call these *topography transfer* and *slipperiness transfer*.

Our convention for the Fourier transform pair is

$$\widehat{f}(k) = \int_{-\infty}^{\infty} f(x)e^{-ikx}\,\mathrm{d}x \qquad \text{and} \qquad F^{-1}\left[\widehat{f}\right] = f(x) = \frac{1}{2\pi}\int_{-\infty}^{\infty}\widehat{f}(k)e^{ikx}\,\mathrm{d}k. \tag{4}$$

Equations (2) and (3) account for the fact that G2003 defined this pair with k having the opposite sign.

To predict response s in this linear theory, one multiplies T_{sb} with the Fourier transform of the topography forcing $b(x)$ and compute the inverse transform (i.e., $F^{-1}[T_{\mathrm{sb}}\hat{b}]$); in contrast, T_{sc} is multiplied with ice thickness H as well as the Fourier transform of the slipperiness forcing $c(x)$ before inversion ($F^{-1}[T_{\mathrm{sc}}H\hat{c}]$). The extra H appears here because the transfer functions relate perturbations and responses on a scaled flow of unit ice thickness; H cancels out in the case of b. The problem is linear, and the responses to the two forcings are summed.

Figure 2 plots the transfer functions against dimensionless wavelength for $\alpha = 3°$, 0.3°, and 0.01°, which may respectively describe the slopes on a valley glacier, an ice sheet, and an ice stream. At intermediate/mesoscale wavelengths, $\lambda/H \sim 1$–10, we see strong influences of basal slip γ on the amplitude of T_{sb} and the phase of both functions. For bed topographic undulations with such wavelengths, low slip causes a subdued response with pronounced phase lead, whereas high slip causes them to be *copied* to the surface with nearly full amplitude and reduced phase difference. The amplitude of T_{sc} becomes large only at long wavelengths ($\lambda/H \gtrsim 10^2$); it is small at mesoscale wavelengths unless α is high, and even then still smaller than the amplitude of T_{sb} for the same slip ratios. Lower slope weakens both transfers in the same way (the denominators of (2) and (3), where α appears, are identical so $T_{\mathrm{sc}}/T_{\mathrm{sb}}$ is independent of slope).

Besides uniform-slab conditions, key assumptions behind this theory are that the forcings and responses have small amplitudes and ice rheology is isotropic with constant viscosity. By comparing its predictions against surface topography computed by finite-element solution of the full Stokes problem, Raymond and Gudmundsson (2005) found that non-Newtonian rheology (e.g., with Glen's exponent $n = 3$) changes the transfers quantitatively, not qualitatively, and T_{sb} and T_{sc} are sufficiently accurate for bed undulation amplitudes up to ~0.5H and slipperiness perturbation amplitudes up to 0.5. By assuming an exponential depth dependence for ice viscosity, Gudmundsson et al. (1998) derived alternative versions of T_{sb} and T_{sc}. To limit the use of parameterizations, however, we employ equations (2) and (3) throughout this paper.

2.2. Nonstationary Transfer Method

T_{sb} and T_{sc} are themselves Fourier transforms of *impulse response functions* in the spatial domain—the responses in s when the forcings are delta functions at $x = 0$. Let these impulse response functions be

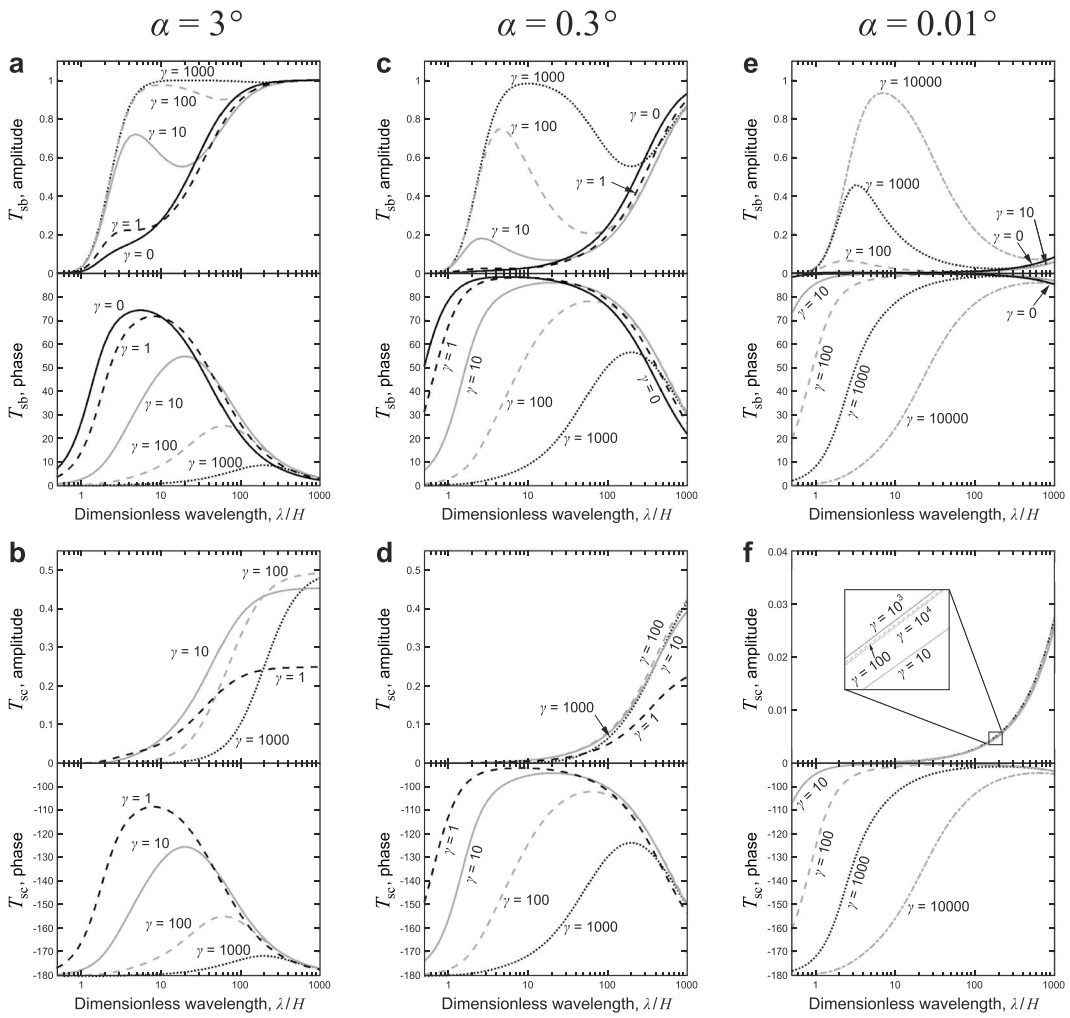

Figure 2. (a, b) Amplitude and phase of the Fourier domain transfer functions (a) T_{sb} and (b) T_{sc} of Gudmundsson (2003) against dimensionless wavelength, for surface slope angle α = 3° and different basal slip ratios γ. Panels (c) and (d) give the same plots for α = 0.3°, and (e) and (f) for α = 0.01°.

$\eta_{sb}(x) = F^{-1}(T_{sb})$ and $\eta_{sc}(x) = F^{-1}(T_{sc})$. Then, in the uniform-slab case, the responses are given by the convolutions

$$s(x) = \int_{-\infty}^{\infty} \eta_{sb}(x-\tau) b(\tau)\, d\tau \tag{5a}$$

and

$$s(x) = \int_{-\infty}^{\infty} \eta_{sc}(x-\tau) Hc(\tau)\, d\tau. \tag{5b}$$

We modify these integrals to derive our method. When the flow is nonuniform, the background variables $H(x)$, $\alpha(x)$ and $\gamma(x)$ influencing the transfers are no longer constant, so T_{sb} and T_{sc} vary with position. If these controls vary slowly, we can assume that the impulse responses resulting from their local values continue to be valid at each position; that is, they approximate the Green's functions. Accordingly, we generalize equation (5a) by writing

$$s(x) = \int_{-\infty}^{\infty} \eta_{sb}(q,p) b(\tau)\, d\tau = \int_{-\infty}^{\infty} \eta_{sb}(x-\tau,\tau) b(\tau)\, d\tau, \tag{6}$$

where η_{sb} has been extended to be a function of two variables: the distance $q = x - \tau$ rendering the spatial

variation of the response, and the forcing position $p = \tau$. Equation (5b) is generalized in the same manner, with $H(\tau)c(\tau)$ in place of $b(\tau)$.

Equation (6) describes a *nonstationary convolution* commonly employed in geophysics for time-dependent filtering of radar/seismic signals (e.g., Margrave, 1998). We are using it to model ice flow transmission for the first time. Given (6), the Fourier transform of s can be written

$$\begin{aligned}\widehat{s}(k) &= \int_{-\infty}^{\infty}\left(\int_{-\infty}^{\infty}\eta_{\mathrm{sb}}(X-x,x)b(x)\,\mathrm{d}x\right)e^{-ikX}\,\mathrm{d}X \\ &= \int_{-\infty}^{\infty}b(x)\left(\int_{-\infty}^{\infty}\eta_{\mathrm{sb}}(X-x,x)\,e^{-ikX}\,\mathrm{d}X\right)\mathrm{d}x \\ &= \int_{-\infty}^{\infty}T_{\mathrm{sb}}(k,x)b(x)e^{-ikx}\,\mathrm{d}x,\end{aligned} \tag{7}$$

which provides our method of computing s from b under nonstationary topography transfer. The integral transform on the right-hand side here is not the Fourier transform but involves G2003's Fourier transfer function, whose variation with x we recognize through its dependence on the background variables. (In the uniform case, equation (7) reduces to $\hat{s} = T_{\mathrm{sb}}(k)\hat{b}$.) With both topographic and slipperiness forcings, the response is

$$\widehat{s}(k) = \int_{-\infty}^{\infty}T_{\mathrm{sb}}(k,x)b(x)e^{-ikx}\,\mathrm{d}x + \int_{-\infty}^{\infty}T_{\mathrm{sc}}(k,x)H(x)c(x)e^{-ikx}\,\mathrm{d}x, \tag{8}$$

and $s(x)$ is found via the inverse Fourier transform of $\hat{s}$:

$$s(x) = \frac{1}{2\pi}\int_{-\infty}^{\infty}\widehat{s}(k)e^{ikx}\,\mathrm{d}k. \tag{9}$$

When gathering inputs for this method, a relevant question is what we classify as *background* variability (which controls the transfer) and what as *perturbations* (forcings and responses) on a flowline. Background variables are meant to vary slowly, so should be long waves; accordingly, perturbations should be short waves. Decomposing variables into these components requires a smoothing filter on a length scale, L. Given our interest in mesoscale undulations ($\lambda/H \sim 1$–10), a threshold length scale of $L/H \approx 10$ to several tens seems appropriate, but its choice is not unique. As we shall see later, the choice is typically informed by the actual variations on a given flowline and subject to practical constraints. *Clean* scale separation may be better satisfied on some flowlines or flowline sections than others, and we expect the method to perform poorly (be more crudely approximate) when strong variations occur on a continuous range of scales. This issue is often encountered when multiple-scale techniques are used in real situations.

Errors in the method stem from three sources: (i) the approximation of the (unknown) Green's functions by η_{sb} and η_{sc}, (ii) the degree of scale separation determining how well a flow can be approximated by transfer of perturbations controlled by background variables, and (iii) the effect of finite-amplitude variations in a linear perturbation theory. (Items (i) and (ii) respectively concern the leading-order and higher-order terms of the multiple-scale asymptotic expansion.)

2.3. Numerical Implementation

Those integrals in equations (7) and (8) cannot be evaluated using standard codes for the Discrete Fourier Transform or Fast Fourier Transform because T_{sb} and T_{sc} are functions of wavenumber as well as position. We compute them by discrete summation: for example,

$$\widehat{s}(k_m) = \sum_{n=1}^{N}T_{\mathrm{sb}}(k_m,x_n)b_n e^{-ik_m(n-1)\Delta x}\,\Delta x, \tag{10}$$

for wavenumbers $k_m = m\Delta k$, $m = 0, 1, \ldots, N-1$, where $\Delta k = 2\pi/N\Delta x$, Δx is the step size, and N is the number of points in the domain (as in the Discrete Fourier Transform). The sum is implemented by matrix multiplication,

with the product of T_{sb} with the exponential expressed as a matrix, and $\hat{s}$ and b as column vectors. The inverse Fourier transform is computed with standard code.

2.4. Wavelet Transform

The spectral contents of forcings and response vary along each flowline. In our experiments, we use the continuous wavelet transform (CWT) to assess them and their relationship. The CWT of a signal $f(x)$ is defined by

$$Wf(p,a) = \int_{-\infty}^{\infty} f(x) \frac{1}{\sqrt{a}} \psi^* \left(\frac{x-p}{a} \right) \mathrm{d}x, \tag{11}$$

where ψ is the mother wavelet (we choose the analytic Morlet wavelet with $\omega_0 = 6$), p is position, a is the scale, and * denotes complex conjugate (Alessio, 2016; Mallat, 2009). Wf is the convolution of f with dilated (conjugated) daughter wavelets. The prefactor $a^{-1/2}$ ensures L2 normalization of wavelet energy. We compute the CWT with the MATLAB function *cwtft*.

The CWT measures the strength of variations in f at different length scales at different positions along flow. Strength is depicted in color on a *scalogram* (e.g., Figure 4), where the horizontal axis is position and the vertical axis is pseudoperiod (equivalent to wavelength λ) derived from the scale a. The strength profile at each position can be roughly interpreted as a power spectrum. To aid readers unfamiliar with this transform, we begin using it in our synthetic flowline experiments, where the signals are relatively simple.

The fact that nonuniform transfer involves position-dependent spectral filtering suggests that it could be carried out in the wavelet domain (p-a space) using *wavelet transfer functions*—akin to those in the Fourier domain—that operate on Wb and Wc to give Ws; taking the inverse wavelet transform then gives $s(x)$. This route turns out to be possible but highly circuitous (Appendix A). We adopt the method of equations (8) and (9) in this paper.

3. Numerical Experiments

The method was tested on three synthetic flowlines (section 3.1 and Figure 3) and two real flowlines (sections 3.2 and 3.3), the latter being the central flowline of Columbia Glacier, Alaska, and a flowline of the Greenland Ice Sheet ending on Nordenskiöld Glacier (Figures 6a and 6b). Our general position is to predict $s(x)$ from input data for the forcings $b(x)$ and $c(x)$ and background variables $H(x)$, $\alpha(x)$, and $\gamma(x)$. We call *s surface perturbation* and *b bed perturbation*, omitting the word *topographic*, for brevity. We label the predicted surface $s_p(x)$ to distinguish it from the observed surface. All flowlines show large background variations that preclude the standard use of G2003's transfer theory.

In the real experiments, the slipperiness forcing $c(x)$ is unknown and we evaluate equation (8) without its second integral to see to what extent topography transfer alone explains the surface undulations. (The possibility of retrieving $c(x)$ is discussed in section 4.2.)

The two real flowlines, though chosen in view of their vastly different ice thicknesses and slopes, are not meant to be *representative* of flowlines on valley glaciers and ice sheets. This concept is not useful because the combinations of H, α, and γ and of their spatial variations on and within different flowlines span a huge parameter space. More exhaustive testing on many flowlines is certainly desirable. While this is not done here given space limitation, a separate study by us (Ignéczi et al., 2018) applies the method to >5,000 flowlines across the Greenland Ice Sheet, examining also the links between their surface undulations and supraglacial drainage features.

3.1. Synthetic Case Studies

We first tested the method on synthetic, steady state glaciers in the (x, z) domain simulated by incompressible Stokes flow with constant viscosity (Figure 3a). The goal is to verify that it works on nonuniform flowlines under the favorable conditions of 2-D, linear viscous flow with completely known basal forcings. How complications degrade its performance is then apparent from the real case studies.

On a finite-element mesh of the glacier in each experiment, the scaled model

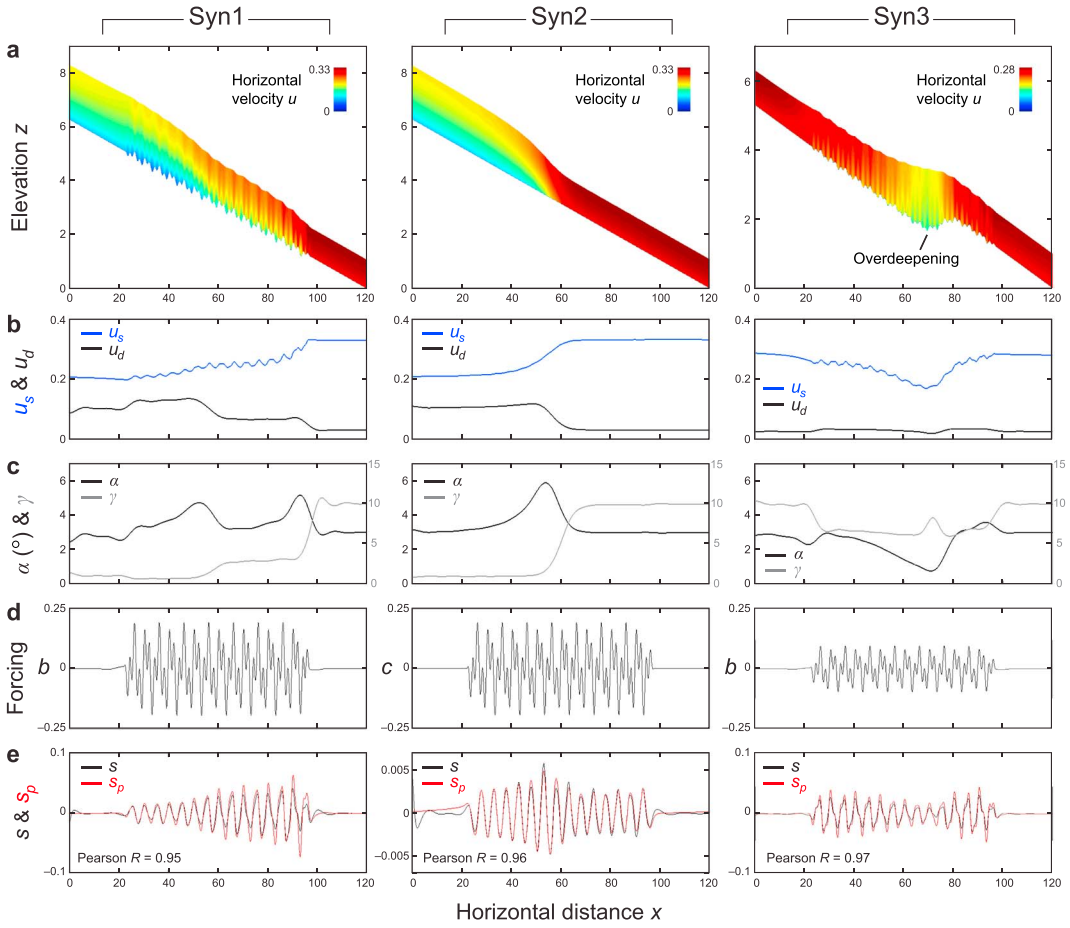

Figure 3. Modeling of bed-to-surface transmission in three synthetic flowline experiments Syn1, Syn2, and Syn3. (a) Geometry and horizontal velocity field of each steady state glacier. (b) Profiles of observed (unsmoothed) surface velocity u_s and estimated deformation velocity u_d. (c) Background profiles of surface slope α and slip ratio γ. (d) Prescribed basal perturbation forcing $b(x)$ or $c(x)$. (e) Observed surface undulations s (x) (the target, in black) and predicted surface undulations $s_p(x)$ (red). All variables are dimensionless, with scales as described in section 3.1.

$$-\nabla P + \nabla^2 \mathbf{u} + \begin{pmatrix} 0 \\ -1 \end{pmatrix} = \mathbf{0}, \qquad \nabla \cdot \mathbf{u} = 0 \tag{12}$$

was solved for the fields of pressure P and velocity $\mathbf{u} = (u, w)$ using the Stokes solver of the MATLAB *QuickerSim CFD Toolbox* (https://quickersim.com). The computed surface velocity and kinematic free-surface condition were used, with zero mass balance, to evolve the ice surface to steady state. Variables are dimensionless, with the length scale $[d]$ for both Cartesian coordinates and all distances and elevations, and the scales $\rho_i g[d]$ for pressure and $\rho_i g[d]^2/\mu_i$ for velocity, where g is gravity, ρ_i is ice density, and μ_i is ice viscosity. At the bed, the sliding law $u_b = C(1 + c)\tau_b$ and no normal penetration were imposed as boundary conditions (as in G2003). Sliding was implemented by the common approach of a thin basal mesh layer (0.01 unit thick) with adjusted viscosity (e.g., Raymond & Gudmundsson, 2005). Upstream and downstream boundaries were set far from the nonuniform stretch to ensure their flow to be parallel with parabolic velocity profiles. We imposed a constant ice flux (thus, constant thickness) at the upstream end. Numerical data of all steady state fields and geometries are given in the repository linked with this paper.

Figure 3 shows the setup of three experiments: Syn1, Syn2, and Syn3. The forcings in Syn1 and Syn3 are a b perturbation only—a sum of two sinusoids with wavelengths $\lambda = 2$ and 5 (Figures 3a and 3d). The forcing in

Syn2 uses the function in Syn1 but is a *c* perturbation (Figure 3d). All forcings were imposed in $x = 25$ to 95. The horizontal grid spacing is $\Delta x = 0.2$. In Syn1 and Syn2, the unperturbed bed is linear with 3° slope, and we set the background sliding parameter $C(x)$ to rise smoothly from 1 to 10 across the central part of the domain to induce background flow acceleration. In contrast, in Syn3 we set $C \equiv 10$ everywhere, as an imposed basal overdeepening already ensures nonuniform flow. Syn1, Syn2, and Syn3 were designed to explore nonuniform topography transfer due to varying slip, nonuniform slipperiness transfer due to varying slip and ice thickness, and nonuniform topography transfer due to varying ice thickness and slope, respectively. But note that the glacier dynamics mean that no single background variable (H, α, and γ) can be held exactly constant across the domain.

Our transfer method was used to predict the surface undulations on these glaciers. The smoothing length scale $L = 10$ (discussed later) was used to extract background variables from their flow. We smoothed each given profile with a sixth-order Butterworth low-pass filter (with cutoff frequency defined by L) to distil its background component, and then subtracted this from the profile to find the perturbation where needed. For the bed and surface topography, the subtraction yields b and s (Figures 3d and 3e). Using thickness H and slope α of the smoothed topography, we calculated the background deformation speed via the parallel-flow formula: $u_d = \sin\alpha(H\cos\alpha)^2/2$. Then, using equation (1), we found the slip ratio γ from u_d and the background (i.e., smoothed) component of the surface speed (Figures 3b and 3c). Figure 3 shows reasonable scale separation between background variables and perturbations in all three experiments.

Figure 3e compares $s_p(x)$ found with our nonuniform transfer method to $s(x)$ in each experiment. The size, shape, and phase of the undulations are reproduced remarkably well, with root-mean-square errors (RMSEs) < 0.01 and Pearson correlation coefficients $R \geq 0.95$. In Syn1 and Syn3, the undulation amplitudes are somewhat overpredicted, probably because b reaches a nonnegligible fraction (~10%) of the ice thickness. This departure from linear response under finite-amplitude forcings is known from the tests of G2003's theory by Raymond and Gudmundsson (2005). Rapid changes on one or more background variables are also expected to worsen the approximation behind our method (section 2.2); indeed, we see signs of a greater mismatch where this happens: for example, in $x = 90$–100 in Syn1 and $x = 50$–65 in Syn2.

Two aspects of the results in Figure 3e affirm our method's ability to estimate nonuniform transfer correctly. The ice flow transmission in each experiment is (i) wavelength-dependent and (ii) modulated by background variations, and s_p convincingly captures both features. Like s, s_p relates weaker transmission of the $\lambda = 2$ forcing than the $\lambda = 5$ forcing; the observed transfer magnitudes at these wavelengths are consistent with $|T_{sb}|$ and $|T_{sc}|$ in the mesoscale region $\lambda/H \sim 1$ to 5 in Figures 2a and 2b. (Note that we can interpret T_{sb} and T_{sc} only approximately for nonuniform flow, and α deviates from 3°, and H from 1, in the experiments.) This selective transmission explains why the surface response shows a dominant $\lambda = 5$ signal with minor wiggles on its undulations. Regarding the modulation effect, the form of $|T_{sb}|$ (Figure 2a) implies stronger topography transfer at higher γ, higher α or lower H (via changing λ/H) for the mesoscale wavelengths of interest. These dependences explain why s and s_p grow in amplitude along flow in Syn1 and attain minimum amplitude above the overdeepening in Syn3 (Figures 3a, 3c, and 3e). The pattern of s in Syn2 is similarly explainable by the slipperiness transfer magnitude $|T_{sc}|$. The undulation amplitude peak at $x \approx 50$–60 (Figure 3e) is due to the ice surface steepening there, which raises $|T_{sc}|$ locally, while $|T_{sc}|$ at $\lambda = 5$ in the areas further upstream (where $\gamma = 1$) and downstream ($\gamma = 10$) are similar when we account for their different ice thicknesses. These experiments and Figure 2 show that the *slipperiness transfer* is much weaker than the *topography transfer* ($|T_{sc}| \ll |T_{sb}|$) at mesoscale wavelengths, including at low slope (Figures 2e and 2f). But we emphasize that the *actual response amplitudes* depend also on the sizes of the forcings b and c, which are not directly comparable (they have different units, and H scales the slipperiness response).

These findings are corroborated by the CWTs of b, c, s and s_p in Figure 4, which analyze the signals spectrally as well as spatially. Here the top panels show the dual-λ compositions of the forcings. The middle and lower panels, which confirm the overall match between s and s_p in the experiments, show their amplitude evolution at $\lambda \approx 5$ across the domain and suppression of their $\lambda \approx 2$ components (notably in Syn2), as discussed above. But these scalograms also reveal a good match between s and s_p at $\lambda \approx 2$ and at long waves ($\lambda \approx 7$–10) that are difficult to discern from Figure 3e. Interestingly, while the s_p-scalograms show a subdued response at

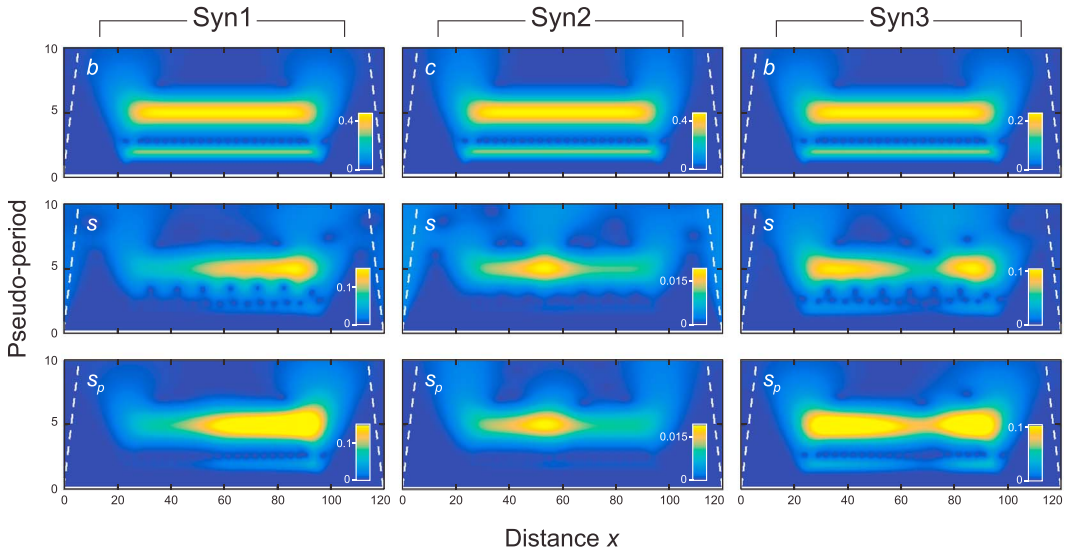

Figure 4. Wavelet transforms (scalograms) of the basal forcing $b(x)$ or $c(x)$, observed surface undulations $s(x)$, and predicted surface undulations $s_p(x)$, in the synthetic experiments. Dashed white lines mark the cone of influence beyond which edge effects maybe prominent.

$\lambda \approx 2.5$–3, the s-scalograms in Syn1 and Syn3 exhibit a spatially oscillatory signal at this wavelength. Its origin is unclear and may stem from interference between the $\lambda = 2$ and 5 components (i.e., beat phenomenon) in the free-surface flow dynamics.

How does the smoothing length L affect these results? And generally, how should we choose L? As our aim is to transfer mesoscale perturbations ($\lambda/H \sim 1$–10), L should be at least an order of magnitude larger than the mean ice thickness $\bar{H}$ (≈1.5 units for our synthetic glaciers), and thus, in the region where the shallow-ice approximation applies. The length scales over which background parameters vary are then consistent with our use of T_{sb} and T_{sc} in the method (recall G2003 derived these for parallel-slab flow) and consistent with the formula for u_d, which De Rydt et al. (2013) also found using a shallow-ice formula in their ice stream work. We chose $L = 10$ for these reasons. Judging from Figure 3, a much greater L is undesirable, as it would smooth the glacier geometries excessively to cause large-amplitude features to appear on b and s, making the linearized theory inaccurate. (In multiple-scale terms, this occurs because L then misses the actual separation between background and variability.) This expectation is confirmed in Figure 5a, which plots the RMSE and Pearson R between s_p and s found from repeating the predictions at different L. When L is increased past ~15, both measures show rapidly rising mismatch. When $L < 5$, we see small RMSEs and relatively high R, but these are misleading because the wavelength range of the forcings being transferred is then severely limited, and the mesoscale undulations at $\lambda = 5$ are cast as background variations, rather than explained. Our L value lies in an optimal region (~7 to 12 units) of high R and low RMSE, and varying it across this region does not alter the predictions substantially. These considerations and experiments show that while L is not unique and varies between flowlines, it is sensible to pick L to be $\gtrsim 10\bar{H}$ and as large as possible so long as the resulting perturbations have small amplitude.

In summary, if these synthetic flowlines were presented to us as real (and we knew the forcing c in Syn2), we would be able to predict their surface undulations successfully.

3.2. Columbia Flowline

Columbia Glacier is a complex temperate tidewater glacier in Southern Alaska's Chugach Range. It has experienced sustained thinning and frontal retreat for over three decades (McNabb et al., 2012; O'Neel et al., 2005), with the snout today lying >20 km upstream of its 1980 position. Given its unsteady behavior, we conducted experiments for two years: 2012 and 2007. This choice is based on the availability of broadly contemporaneous and spatially complete topographic and flow-speed data, and the opportunity for comparative analysis.

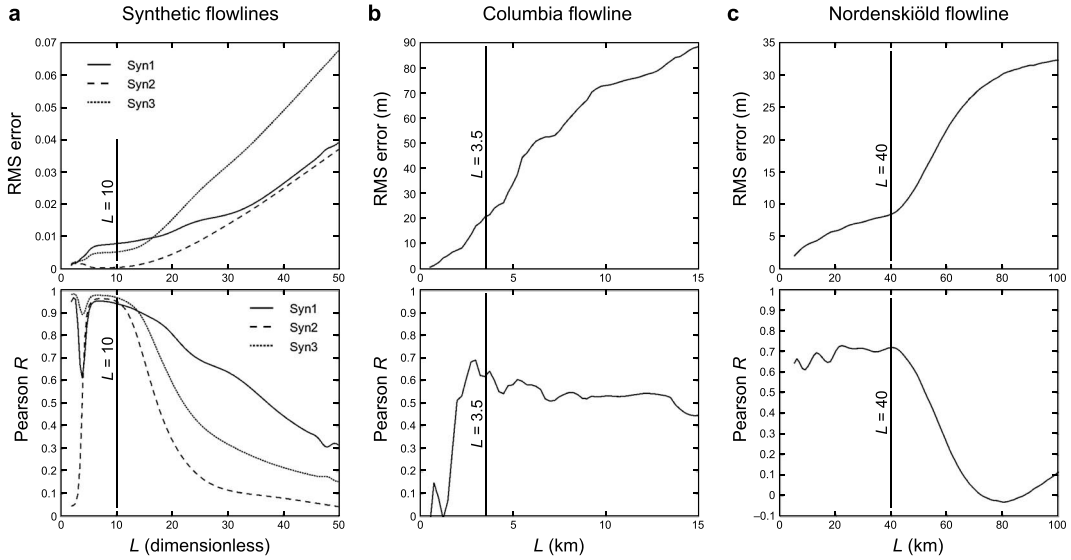

Figure 5. Dependence of the root-mean-square (RMS) error and Pearson correlation coefficient R between $s_p(x)$ and $s(x)$ on the smoothing length scale L in the (a) synthetic, (b) Columbia, and (c) Nordenskiöld flowline experiments. Vertical lines mark our chosen values of L.

3.2.1. Data Compilation

Figure 6 introduces relevant data. We use updated coordinates for the central flowline on the glacier's main branch provided by R. W. McNabb (Figure 6a). The bed topography along this (Figure 6c) was extracted from the digital elevation model (DEM) of McNabb et al. (2012), which has a 100-m grid resolution and 5-m mean absolute error and 44-m RMS error in terms of ice thickness. The 2012 surface profile along the flowline (provided to us at 0.5-km spacing by McNabb) is derived from the State of Alaska's interferometric synthetic aperture radar DEM (https://lta.cr.usgs.gov/IFSAR_Alaska); the 2007 surface profile is derived from the 40-m resolution SPOT (Satellite Pour l'Observation de la Terre) DEM (Korona et al., 2009). Bilinear interpolation was used in the extractions. All profiles were compiled at or resampled to the horizontal step size $\Delta x = 50$ m. On the flowline, the mean ice thickness is ≈350 m and surface slope (α) fluctuates in the 0–10° range (Figure 6e). Thinning occurred on the lower glacier and frontal retreat shortened the flowline (≈50 km long) between 2007 and 2012. Despite these changes, similar undulations can be seen on the surface in both years (Figures 6c and 7c).

At each position, equation (1) was used to find slip ratio γ from the smoothed (observed) surface flow speed u_s and deformation speed u_d. The latter was estimated using the formula

$$u_d = \frac{2A}{n+1}(\rho_i g H \sin\alpha)^n H \tag{13}$$

based on Glen's flow law (Cuffey & Paterson, 2010, p. 310). We prescribed $n = 3$ (Glen's exponent), $A = 2.4 \times 10^{-24}$ Pa^{-3}s^{-1} (creep parameter for temperate ice) and data for H and α derived from the elevation profiles smoothed at $L = 3.5$ km (justified shortly). To avoid negative slip, we set γ to zero where $u_d > u_s$. In areas of zero/reversed surface slope, γ becomes infinite but is capped at 10^5 in our computation.

Columbia Glacier exhibits seasonal cycles in its motion, with flow speeds on the main branch peaking in spring and reaching a minimum in the late summer/autumn (Meier et al., 1985; Vijay & Braun, 2017). Different profiles of u_s in the slip ratio calculation are possible. In the 2012 experiment, we used representative maximal and minimal speed profiles from spring and autumn, rather than an annual-mean speed profile (which would require estimation), in order to assess uncertainty around the predictions and the impact of flow acceleration/deceleration on the transmission. Specifically we used u_s data along the centerline for March 2011 and October 2011 (curves labeled *2011 SPR* and *2011 AUT*, Figure 6e) derived by feature/speckle-tracking on TerraSAR-X synthetic aperture radar data; the associated errors are on the order of 1–10 m/year (McNabb et al., 2012). We lack similar-quality data for 2012, hence our decision to use profiles

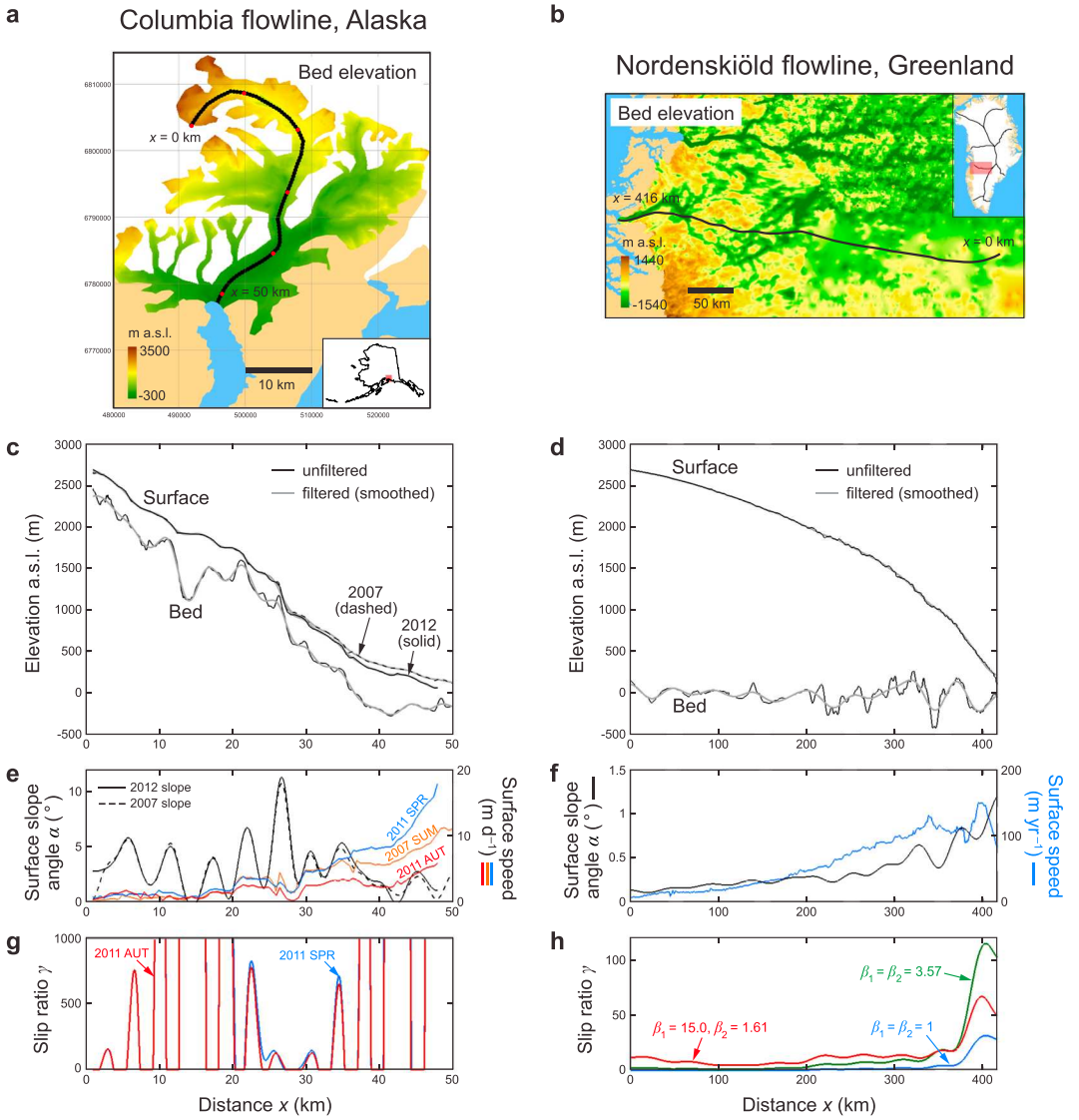

Figure 6. Model input data for the Columbia flowline (left) and Nordenskiöld flowline (right) experiments. (a, b) Flowline locations and bed elevation maps. (c, d) Along-flow profiles of surface and bed elevation (black) and smoothed counterparts (gray). Surface elevations for Columbia Glacier in 2007 and 2012 are used. (e, f) Profiles of ice surface slope and flow speed. Flow speeds on Columbia Glacier in 2007 June/July (*SUM*: Summer) and 2011 March (*SPR*) and 2011 October (*AUT*) are shown. Flow speeds on the Nordenskiöld flowline derive from MEaSUREs composite for 2000–2010 (Joughin et al., 2010). (g, h) Profiles of slip ratio γ used in our modeling.

from 2011. In the 2007 experiment, we employed u_s data derived for June/July 2007 from Landsat TM/ETM+ imagery (*2007 SUM*, Figure 6e), whose processing used a branched version of pycorr (Fahnestock et al., 2016). This speed profile, the only available to us for 2007, lies between the 2011 profiles and probably resembles the 2007 annual mean. All speed profiles described here were computed by R.W. McNabb and provided to us at 0.5-km spacing.

3.2.2. Smoothing and Decomposition of Input Profiles

Background variables and perturbations were extracted from the topographic and speed data by the filtering procedure described in section 3.1. Given the insights from the synthetic studies, we chose the smoothing length scale L based on the opposing interests of maximizing the wavelength range to be studied for nonuniform transfer ($2\Delta x \lesssim \lambda \lesssim L$) and keeping perturbations b and s small. The latter poses a strong upper limit for the Columbia flowline, forcing us to specify L = 3.5 km ($\approx 10\bar{H}$), the minimum acceptable. Consequently, the mesoscale range is limited to $0.1 \lesssim \lambda \lesssim 3.5$ km in our experiments.

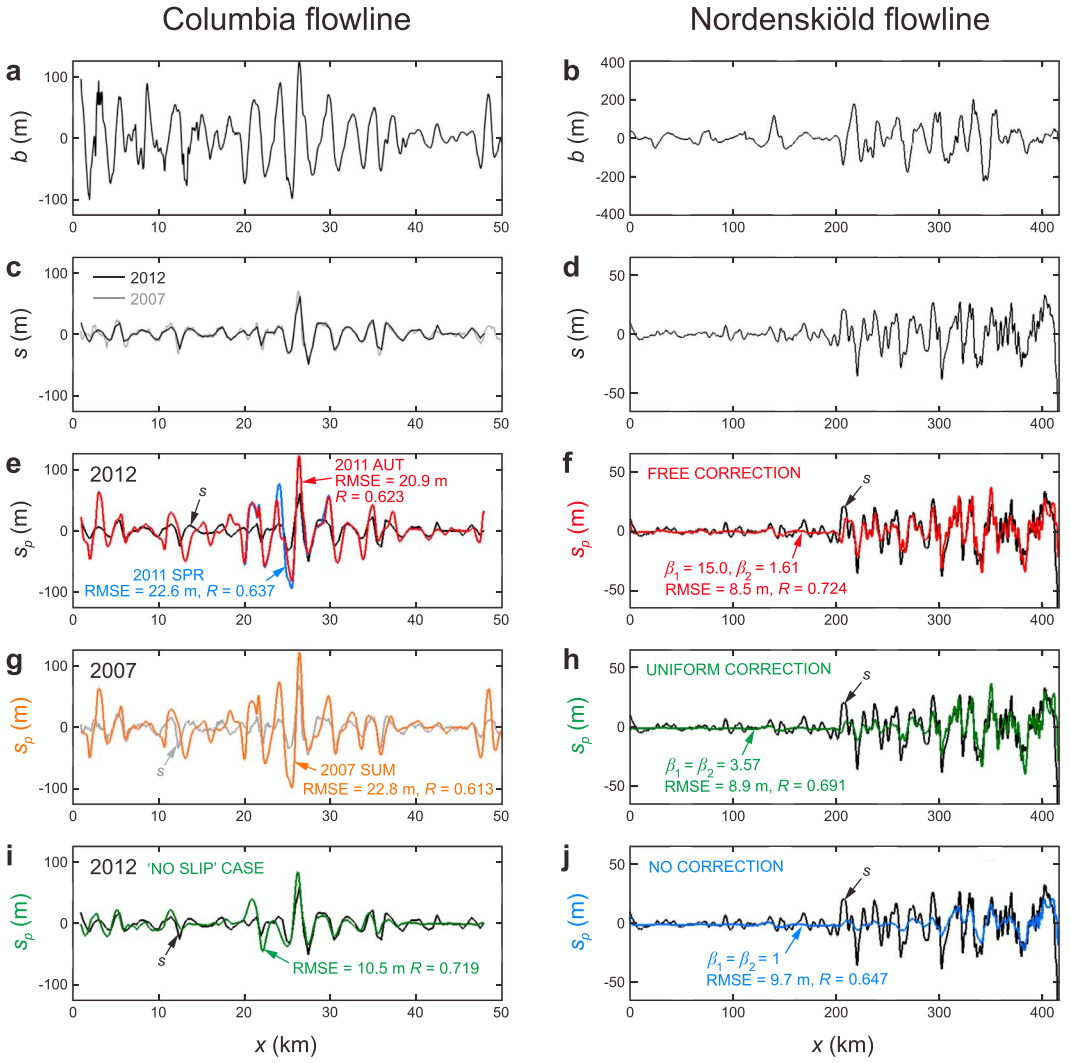

Figure 7. Model predictions of bed-to-surface transmission on the Columbia flowline (left) and Nordenskiöld flowline (right). (a, b) Bed topographic forcing $b(x)$. (c, d) Observed surface perturbation $s(x)$. (e–j) Predicted surface perturbation $s_p(x)$ in different runs. Root-mean-square error (RMSE) and Pearson correlation R between $s_p(x)$ and $s(x)$ are indicated.

Figure 6c shows the background topography $S(x)$ and $B(x)$, and Figures 7a and 7c the bed and surface perturbations. The perturbation $b(x)$ contains features verging on too large a fraction of the ice thickness, notably at km 21 and km 27 where the glacier thins markedly. Increasing L worsens this outcome. Low L here means that relatively short-scale variability is classed as perturbations; the bed-topographic peaks and troughs with wavelengths of 5–10 km visible in Figure 6c are not extracted, as their amplitudes are too large to be addressed by the linearized theory.

Figure 6g plots the slip ratios $\gamma(x)$ for 2011 spring and autumn (results for 2007 lie amid them and are omitted for clarity). Even after smoothing, these profiles show sharp changes between high and no slip and regions of infinite slip. This example highlights a problem when inputs fluctuate strongly. We apply the method nonetheless and discuss this issue later.

3.2.3. Results and Analysis

The perturbations $b(x)$ and $s(x)$ undulate with similar dominant periods of several kilometers and amplitudes of ~100 and ~20 m, respectively (Figures 7a and 7c). The undulations on s hardly changed from 2007 to 2012, attesting they were real, stable features. Visible correlation between the peak-trough sequences on b and s evidences ice flow transmission, although individual peaks/troughs are often misaligned, indicating a phase shift, with b lagging behind s. Packets of larger cycles occur over similar stretches (km 1–12; km 21–36) on

both perturbations. This inspection emphasizes the longer/larger cycles, not the smaller/shorter superimposed variations.

As noted before, our method is used here to predict s_p assuming topography transfer only, because the slipperiness forcing c is unknown. Figures 7e and 7g plot s_p for 2012 (red/blue curves, forced with autumn/spring slip ratios) and 2007 (orange curve) alongside s of those years. These predictions portray a succession of peaks and troughs closely resembling the observed ones in position and pacing, but their amplitudes are overestimated on the two stretches identified above. Still, these results show that our method can predict the qualitative features of $s(x)$.

Higher slip should enhance the topography transfer (section 2.1). This is confirmed by the 2012 experiments, where the lower flow speeds in autumn than spring result in slightly smaller undulations on s_p. In these autumn-/spring-forced runs, the RMSEs between s_p and s are 20.9 m and 22.6 m, respectively; the corresponding Pearson R's are 0.623 and 0.637, so s_p captures about 40% of the variance in s. Using annual-mean speeds to derive slip ratios will not improve upon the autumn result, as they would exceed the autumn speeds. The 2007 run (Figure 7g; RMSE = 22.8 m), forced by summer flow speeds, illustrates this.

In these three experiments, much of the mismatch between s_p and s stems from overprediction of the undulations' size in km 1–12 and km 21–36 (their phase is rather well reproduced). While the overlarge undulations on $b(x)$ at km 21 and 27 presumably generate mismatch, we query what causes overprediction elsewhere. Because switching off sliding reduces the topography transfer, we first performed another run with $\gamma \equiv 0$ to see how much this offsets the overprediction. It improved the match substantially (Figure 7i; RMSE = 10.5 m, R = 0.719). However, we do not consider it likely that our slip ratios were overestimated, because our autumn-forced 2012 experiment assumed minimal surface flow speeds to derive slip ratios, and because accounting for lateral drag on glacier flow would lower our u_d estimates and raise slip ratios further. In other words, the observed flow speeds on Columbia Glacier cannot be explained without fast sliding under parts of the glacier (Figures 6e and 6g): $\gamma \equiv 0$ is unrealistic and the no-slip experiment cannot describe the transmission correctly. Consequently, we infer that the overprediction is due to fundamental limitations of the present method. Relevant causes include (i) nonlinear ice rheology; (ii) 3-D flow effects arising from the trough-shaped bed topography, proximity of lateral shear margins (the glacier is ≈3–6 km wide) and tributaries entering the main branch (Figure 6a); and (iii) surface processes that attenuate surface undulations. Moreover, (iv) the unknown slipperiness forcing c may cause a response that explains some of the discrepancy between s_p and s. Figure 2b shows that on the steeper sections of the glacier where $\alpha \sim$ several degrees, we may expect $|T_{sc}| \sim 0.05$ for the wavelengths of interest ($\lambda \approx 2.5$ km or $\lambda/H \approx 5$–10). Assuming c to be of order 1, the slipperiness transfer can cause undulations reaching $|T_{sc}|cH \sim 20$ m in amplitude. These limitations are discussed in section 4.

To study the results spectrally, we compare the CWTs of b, s, and s_p in the 2012 autumn-forced and the no-slip experiments (Figures 8a–8d). At long pseudoperiods/wavelengths (≈2–3.5 km) on all four scalograms, we see signals around km 2–14 and km 21–36 reflecting the larger undulations noted before. In these stretches, the match in CWT strength and pattern between s and s_p in the no-slip case, and the overestimated strength of s_p in the 2012 experiment, confirm our earlier findings. The scalograms show different details at shorter wavelengths too. In Figure 8b, light blue tongues at $\lambda \sim 1$ km protruding toward the x axis reveal some short-scale variability on s. While s_p in the 2012 autumn experiment carries signals in the same area (Figure 8c), s_p in the no-slip experiment generally lacks them (Figure 8d). Although this difference is subtle, revisiting Figure 7 shows that the sliding experiments indeed predict more fine-scale variations on $s_p(x)$, whose presence on s is confirmed by the 2007 surface derived from the 40-m SPOT DEM (Figures 7c and 7g). The no-slip experiment apparently underestimates the short-scale transfer, besides producing no response in km 39–46 (Figure 8d); that its visually pleasing match in Figure 7i has these deficiencies supports our conclusion that the no-slip assumption is untenable.

We also examine the predicted phase of the surface response on *wavelet-coherence* plots (Figures 8e and 8f). These plots use arrows to indicate the phase misalignment between undulating signals in s_p and s at different wavelengths, wherever the correlation between these signals (coherence) exceeds 0.7. A right-pointing arrow means perfect alignment. The no-slip experiment performs better than the 2012 autumn-forced experiment in $\lambda \sim 2$ to 3.5 km, but worse in $\lambda \sim 1$ to 2 km, which again highlights its short-wave deficiency.

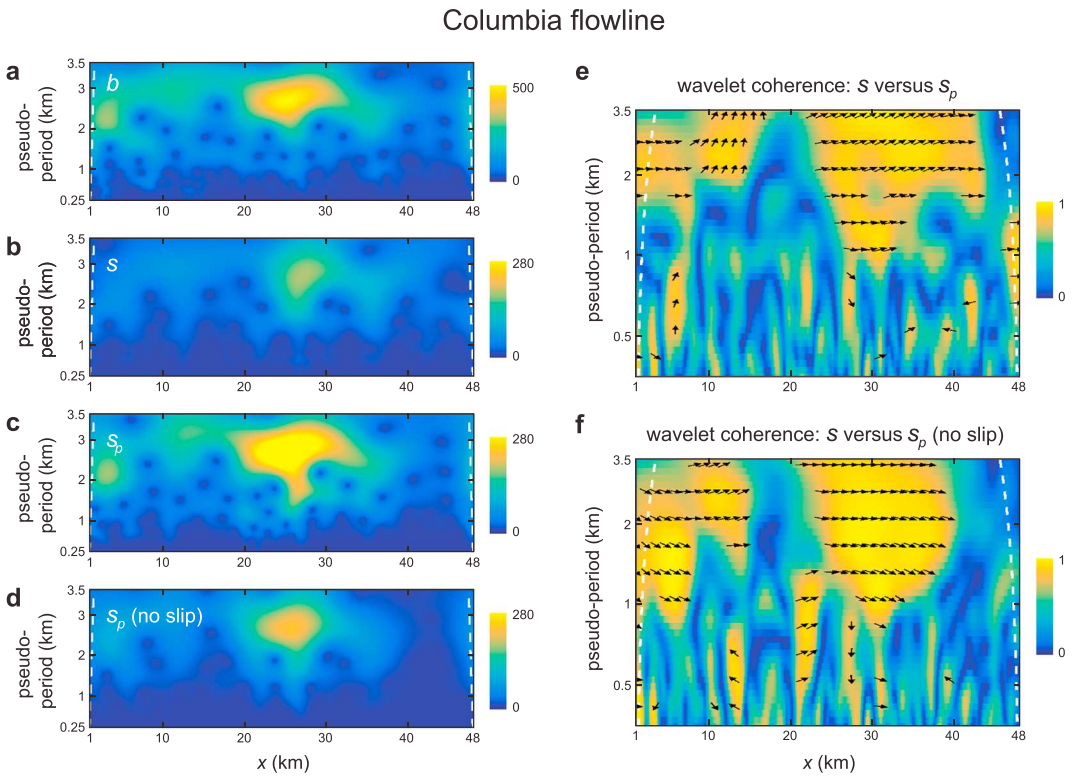

Figure 8. Wavelet transforms of (a) bed topographic undulations $b(x)$, (b) observed surface undulations $s(x)$, (c) predicted surface undulations $s_p(x)$, and (d) $s_p(x)$ with sliding ignored, for the Columbia profile. (e, f) Plots of wavelet coherence between s and the predictions in (c) and (d), with pseudoperiod on log-2 scale. Where coherence level exceeds 0.7, arrows depict the phase error by how much their azimuth deviates from east; that is, right-pointing arrow indicates zero error. Dashed white lines mark the cone of influence beyond which edge effects become prominent.

Not surprisingly, both experiments perform poorly at $\lambda < 1$ km, because the spatial resolution of the 2012 surface elevation data is 0.5 km.

The impact of changing L in the 2012 autumn-forced experiment is shown in Figure 5b. Our L value is a reasonable choice as it yields a Pearson R near the maximum achievable and relatively low RMSE. As expected, raising L worsens the prediction by retaining more large-amplitude undulations on b, which frustrate the linear theory.

3.3. Nordenskiöld Flowline

This flowline, 416 km long, starts from the Greenland Ice Sheet's central divide and ends on Nordenskiöld Glacier, an outlet glacier on the ice sheet's western margin (Figure 6a). We traced it using the velocity field of the ice sheet model validation framework by Price et al. (2017) and extracted its surface elevations from the MEaSUREs Greenland Ice Mapping Project DEM from GeoEye and WorldView Imagery Version 1 data set (Howat et al., 2014, 2017; 30-m grid resolution) and bed elevations from the IceBridge BedMachine Greenland Version 2 data set (Morlighem et al., 2014, 2015; 150-m grid resolution). These data and the slip ratios discussed below were sampled at every 250 m (= Δx) on the flowline.

Along flow, surface speeds increase from several meters per year in the interior to ≈120 m/year near the margin, and ice thickness decreases from 2,500 m to a few hundred meters, so a parallel-slab idealization is invalid; surface slopes are ≈1° or less (Figure 6f). The flow traverses a rough landscape of subglacial mountains and interconnected valleys (Figures 6b and 6d). In $210 \lesssim x \lesssim 370$ km, a detailed bed topography is retrieved by the BedMachine optimization constrained by dense airborne radar soundings measurements, with elevation errors ≲100 m (Morlighem et al., 2014, Figure S6; Figure 2 at https://nsidc.org/data/idbmg4). Due to scarce measurements, the topography is considerably less certain (errors >200 m; Morlighem et al., 2014) in the

first 210 km of the flowline, as is apparent from its smooth appearance there compared to areas further north (Figure 6b).

The bed and surface profiles were decomposed into background and perturbation components, and the smoothed topography used to find H and α, as before. For Nordenskiöld, we specified a large smoothing length scale L = 40 km ($\approx 20\bar{H}$) because the resulting bed and surface undulation amplitudes are still much smaller than H. ($L > 45$ km causes visible problem on the last 30 km of the flowline.) Thus mesoscale variability over a wide spectrum ($0.5 < \lambda < 40$ km) is classified as perturbations.

Unlike in the Columbia case, compiling slip ratios for the Nordenskiöld flowline presents a challenge because most ice in the section is presumably cold. Here, estimating u_d with a Glen-based description requires the local vertical profile of ice temperature T, which controls the creep parameter A. In this ice sheet sector, we expect T near the divide to be as low as ≈ -20 °C through the upper part of the ice column and increase toward the bed due to geothermal heat influence, and T to rise with distance from the divide but remain subzero at intermediate depths. Borehole temperature measurements on Isunnguata Sermia (an outlet glacier 145 km further south) made within 50 km of the margin (Harrington et al., 2015) show that the ice column's top and bottom parts may be temperate in the ablation zone, and the whole column temperate at the margin. Temperature measurements are lacking on/near our flow section, and modeling its thermal structure (e.g., Meierbachtol et al., 2015) is beyond our scope, so we cannot estimate u_d and γ easily.

Given this uncertainty, we conjectured a range of slip ratio profiles for our experiments. MacGregor et al. (2016) recently calculated a conservative map of u_s/u_d for the Greenland Ice Sheet using topographic and u_s data together with equation (13)—assuming the A value for *temperate ice*. Since A increases strongly with T, for example, it is ≈10 times less at −15 °C than at 0 °C (Cuffey & Paterson, 2010), their u_d is overestimated, so their map underestimates the true slip by a factor that increases towards the cold ice sheet interior. We compiled $\gamma(x)$ profiles by multiplying their u_s/u_d data (sampled along the flowline) by the spatial correction factor

$$\beta(x) = \beta_1 + (\beta_2 - \beta_1)\frac{x}{x_{max}} \tag{14}$$

before smoothing and subtracting 1 (see equation (1)). This correction is linear, and β_1 and β_2 define its levels at x = 0 and x_{max} (416 km); our thermal considerations above suggest $\beta_1 \sim 10$ and $\beta_2 \sim 1$. We conducted three different experiments and compared their prediction skills:

1. *Free correction*: β_1 and β_2 are varied to find their optimal combination yielding best fit (minimum RMSE) between $s_p(x)$ and $s(x)$.
2. *Uniform correction*: Best fit optimization was done with $\beta_2 = \beta_1$ ($\equiv \beta$).
3. *No correction (no optimization)*: $\beta_1 = \beta_2 = 1$ ($\equiv \beta$).

3.3.1. Results and Analysis

Figure 7 presents these experiments' inputs and results. The surface perturbation (Figure 7d) shows more short-wave variability than the bed perturbation (Figure 7b), indicating wavelength-dependent transmission. Undulations have amplitudes of ~200 m and tens of meters, for b and s, respectively and appear well correlated in $x > 200$ km where the dominant λ is 10–30 km. The predicted responses in Experiments 1–3 are shown in Figures 7f, 7h, and 7j. Rising trends in their slip ratio profiles (Figure 6h) indicate increasing basal lubrication or a switch from cold to temperate basal conditions along flow (either is consistent with our understanding of thermal regime). The steep rise in slip ratio in $x > 370$ km reflects acceleration of the ice flow as it overtops a ridge to enter the Nordenskiöld subglacial valley (Figure 6b).

In Experiment 1, which yields the most successful prediction, the match between s_p and s has a RMSE of 8.5 m and Pearson R of 0.724 (Figure 7f). Over $210 < x < 370$ km, where the bed topography is most reliable, s_p convincingly mimics the detailed undulations on s at $\lambda \sim$ several kilometers, as well as the broader-scale peaks/troughs on which they reside. The optimal correction parameters β_1 = 15.0 and β_2 = 1.61 in this experiment confirm our thermal expectation. While the large β_1 implies strong amplification of MacGregor et al.'s (2016) u_s/u_d data near the divide—thus, a substantially cold ice column there, $\beta_2 \sim 1$ suggests the column near the margin to be near temperate. At the ends of the stretch of interest, β = 8.2 (210 km) and 3.1 (370 km); the tilted correction results in a roughly constant slip ratio of $\gamma \approx 13$ across the stretch (Figure 6h, red). In contrast, the slip ratios in Experiments 2 and 3 are smaller for the same stretch due to their low

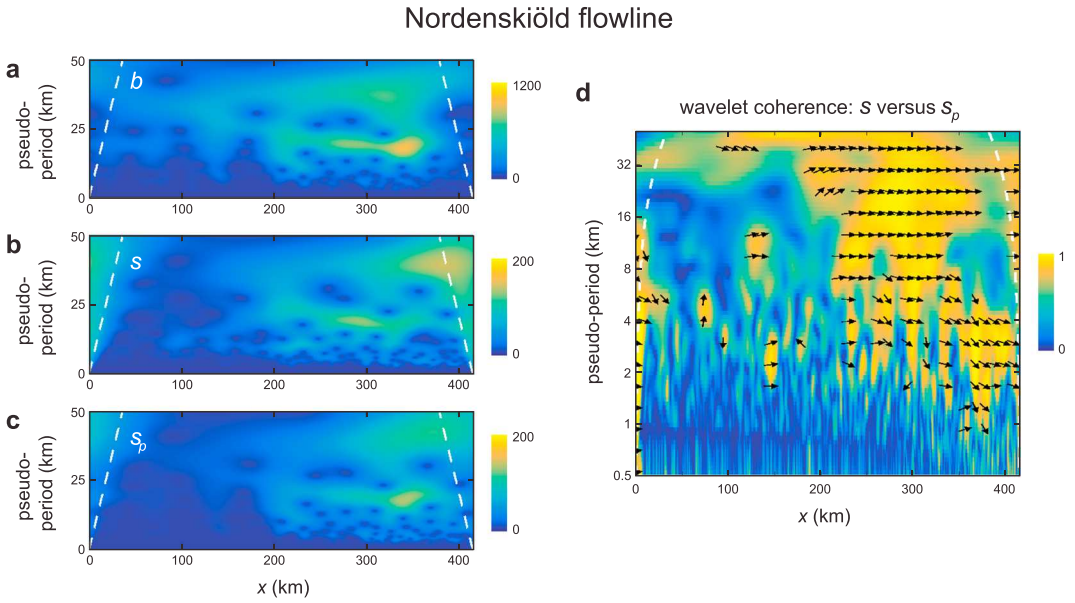

Figure 9. Wavelet transforms of (a) bed topographic undulations $b(x)$, (b) observed surface undulations $s(x)$, and (c) predicted surface undulations $s_p(x)$ in the free-correction prediction experiment, for the Nordenskiöld profile. (d) Plot of wavelet coherence between s and s_p. Where coherence level exceeds 0.7, arrows depict the phase error by how much their azimuth deviates from east. Dashed white lines mark the cone of influence beyond which edge effects become prominent.

β-values—3.57 and 1, respectively. The correspondingly weaker transmissions explain why they predict progressively fewer fluctuations on s and even fail to capture its broad features (Figures 7h and 7j). We also performed a *no slip* experiment ($\gamma \equiv 0$); then s_p is similar to that in Experiment 3 but shows even fewer short undulations, as can be expected from the effect of reduced sliding on transmission. Closer examination reveals that Experiment 1 underestimates details on the upstream part of the stretch, not its downstream part (Figure 7f). This suggests that a nonlinear amplification (with β enhanced more upstream) may better represent the true slip pattern than equation (14).

In Experiment 2, the optimal β ($\equiv 3.57$) is less than the β needed in Experiment 1 to enhance the topography transfer in $210 < x < 300$ km for a good prediction there. A larger β is not found because raising its value degrades the fit near the downstream end of the flowline; thus, the optimization in Experiment 2 is constrained because the RMSE weighs all parts of the domain equally. The optimization in Experiment 1 is less restricted given its extra degree of freedom.

In $x < 210$ km, all three experiments yield subdued responses that underpredict the variability on $s(x)$ and miss most of its peaks and troughs. Thicker ice here ($H > 2$ km) compared to downstream means that bed undulations have shorter dimensionless wavelengths (λ/H) so the topography transfer is weaker, but our method accounts for this factor. A likely reason for the underestimation is that $b(x)$ here is missing real details due to inadequate radar-sounding measurements of bed elevations. Also, with thicker ice, some of the observed undulations might be due to the unknown slipperiness forcing ($|T_{sc}| \sim 0.01$ at $\lambda \approx 20$ km, $\alpha \sim 0.3°$ and $\gamma \sim 10$ from Figure 2d, so that $|T_{sc}|cH \sim 20$ m).

Wavelet analysis shows that, on $b(x)$ and $s(x)$, the pronounced undulations in $x > 210$ km are in fact characterized by two modes of variability at $\lambda \sim 20$ km and $\lambda \sim 35$–45 km (Figures 9a,b). In Experiment 1, s_p captures both modes and the changing spectral composition of s across this region very well (Figure 9c, cf. Figure 9b). These scalograms confirm its poor prediction skill in $x < 200$ km; notably, the emergent signals on s in $x = 80$–180 km, with $\lambda \sim 10$–20 km, are absent from s_p. This dichotomy between the two halves of the flowline, which we suspect is due to erroneous bed topography for the upper half, is unmistakable on the wavelet-coherence plots also (Figure 9d). In $x > 200$ km, long surface undulations with $\lambda > 6$ km are predicted with excellent phase alignment, but shorter undulations have misaligned phases. Going from km 370 to km 210, we also see an increase in the minimum λ where coherence level exceeds 0.7 (Figure 9d). This trend

may be due to degrading accuracy of the bed in this direction and/or increased significance of other processes influencing the mesoscale surface topography (e.g., variations in surface mass balance) as thicker ice attenuates the topography transfer for short waves.

We also repeated Experiment 1 with different smoothing lengths L without changing β_1 and β_2 (i.e., the same thermal structure is assumed for the flow). Figure 5c shows that our L-value lies at the top end of a region of stably high Pearson R. Although decreasing L to 20 km ($\approx 10\bar{H}$) lowers the RMSE, this substantially limits the λ range of the mesoscale transfer.

4. Discussion

In a nonuniform flow setting, how well do the 2-D transfer functions of G2003 predict surface undulations? Our synthetic flowline experiments confirm the validity of the nonstationary transfer method employing these functions. The real case studies show that when complicating factors are present, the method is less accurate as one may expect, but still has explanatory power. Our best prediction runs—the 2012 autumn experiment on the Columbia flowline and Experiment 1 on the Nordenskiöld flowline—reproduce 40% to 50% of their observed mesoscale surface variability (Figures 7e and 7f). By recalling their different aspects, here we gather ideas about the bed-to-surface transmission and the method's applicability and anticipate research avenues.

4.1. Cause of Surface Undulations on the Real Flowlines

A first point to make is that in the real case studies, the method suffers diverse limitations so we cannot hope for exact match between s_p and s. Besides the limitations discussed later (section 4.2), our calculation ignores extraneous mechanisms that cause or modify undulations, for example, nonuniform surface mass balance due to wind-driven processes, albedo variations, or coupling between atmosphere and surface topography. Such mechanisms may have biased the optimisation in the Nordenskiöld runs, and neither equation (8) nor G2003's theory involves mass balance. That surface processes can create mesoscale undulations is evidenced, for instance, by the fields of megadunes in central Antarctica with spacing of a few to ~10 km (Fahnestock et al., 2000), and pronounced spatial variations in snow accumulation on similar length scales and correlated with surface slopes near Talos Dome, East Antarctica (Frezzotti et al., 2007).

Despite this, we conclude that the method is capturing the bed-to-surface transmission more or less correctly, because s_p predicts undulations with size, shape, and sequence like the observed—remarkably well in some places, even if not everywhere. It follows that numerous undulations on our real flowline must owe their origin to topography forcing (as our runs ignore slipperiness forcing), and rapid sliding activates some of them. The transfer function characteristics for $\alpha = 3°$ and $\alpha = 0.3°$ (Figure 2), which roughly describe the surface slopes on the Columbia and Nordenskiöld flowlines respectively, show that $|T_{sb}|$ becomes large at high slip ratios across the corresponding ranges of mesoscale wavelengths being studied—$2/7 \lesssim \lambda/H \lesssim 10$ and $1/4 \lesssim \lambda/H \lesssim 20$. In contrast, the slipperiness transfer magnitude $|T_{sc}|$ is much weaker over these wavelengths (Figures 2b and 2d); but, as explained in sections 3.2 and 3.3, high surface slope and/or thick ice may still enable a slipperiness response (~$|T_{sc}|cH$) that explains some of the remaining mismatch between s_p and s. (We distinguish the meanings of *transfer* and *response* as before.) On flow sections with very low slopes, such as found on Antarctic ice streams and some outlet glaciers in Greenland, $|T_{sc}|$ is even smaller in the mesoscale range (e.g., Figure 2f). In this case, a surface response dominated by slipperiness forcing can arise if the ice is very thick and/or an exceedingly smooth bed ($b \approx 0$) preconditions a minimal topography transfer. Since thicker ice reduces $|T_{sc}|$ at each wavelength (by decreasing λ/H), we expect such response to show larger amplitude and be more noticeable at longer wavelengths.

4.2. Estimating the Slipperiness Forcing

Can we derive $c(x)$ in order to complete the input prescriptions to our method? $c(x)$ quantifies short-scale perturbations of the basal-sliding boundary condition of ice flow, as governed by subglacial processes such as drainage and till mechanics. Accordingly, finding c requires observations/measurements or a physical model of these processes. Both of these approaches are intensely researched; the latter is necessary where our method is used to predict surface undulations in palaeo/future ice flow simulations. To our knowledge, a sound physical model for $c(x)$ is currently out of reach.

However, for present-day ice flow with the right observations, it should be possible to estimate $c(x)$ through an inversion to constrain basal stress/sliding conditions, as has been tackled by Sergienko and Hindmarsh (2013) in a 3-D numerical model. We outline this idea in our context of linearized, nonuniform transfer along flowlines—for future study. Equation (8) predicting surface undulations can be supplemented with a similar equation predicting the perturbation in surface speed, that is,

$$\widehat{s}(k) = \int_{-\infty}^{\infty} T_{\mathrm{sb}}(k,x) b(x) e^{-ikx}\, \mathrm{d}x + \int_{-\infty}^{\infty} T_{\mathrm{sc}}(k,x) H(x) c(x) e^{-ikx}\, \mathrm{d}x, \tag{15}$$

$$\widehat{u}(k) = \int_{-\infty}^{\infty} T_{\mathrm{ub}}(k,x) U(x) b(x)/H(x) e^{-ikx}\, \mathrm{d}x + \int_{-\infty}^{\infty} T_{\mathrm{uc}}(k,x) U(x) c(x) e^{-ikx}\, \mathrm{d}x, \tag{16}$$

where T_{ub} and T_{uc} are Fourier transfer functions describing the transmission of topographic and slipperiness forcings to generate perturbation u on the background surface speed U. (These transfer functions are present, but not listed explicitly, in G2003's theory.) Given data for u_s (filtered to extract u and U) as well as for b, s, and the background geometry, equations (15) and (16) form an inverse problem allowing $c(x)$ to be found, for example, via control methods (MacAyeal, 1993). Optimal estimation with the pair of equations is needed, because $\hat{s}$ and $\hat{u}$ are expected to be weakly sensitive on c (especially at small λ) and the bed topography has uncertainty. Note that this approach retrieves $c(x)$ at a given time only. Ultimately, we need robust models of subglacial processes to predict its temporal evolution.

4.3. Theoretical and Practical Limitations

On what kind (or what parts) of real flowlines do we expect our integral method to predict undulations accurately? Under what circumstances would it underperform? To address these questions, we review its limitations alongside findings from the case studies.

Limitations stem from its *linearity* and *two-dimensional*, *steady flow* assumptions. Departure from conditions compatible with these hampers the method, as is demonstrated by the different prediction accuracies between the synthetic ($R > 0.9$) and real experiments ($R \sim 0.6$–0.7).

Considering linearity first, equation (8) is approximate because T_{sb} and T_{sc} (in (2) and (3)) come from a perturbation theory assuming small-amplitude variability and constant ice viscosity, and because the nonstationary convolution approximates the actual transfer (the Green's function approximation; section 2.2). For these approximations to hold, background variables should vary slowly with x, and s and b be small compared to H. A key case where prediction succeeds because these requirements are met is found in $x > 210$ km in the Nordenskiöld experiment (Figure 7f). The Columbia experiments often violate these requirements, yielding worse prediction due to rapid variations in α and γ (Figures 6e and 6g) and large bed undulations compared to the local ice thickness at km 21 and 27 (section 3.2), which must cause more nonlinear effects. How rheological anisotropy and nonlinearity (nonconstant ice viscosity due to its stress/temperature dependence) affect the surface response is more difficult to analyze. However, as noted before, numerical simulations by Raymond and Gudmundsson (2005) show that nonlinear viscosity tends to cause minor deviations to the response, rather than a fundamentally different response.

Lateral variations in the background flow state (e.g., nonzero lateral shear, flow curvature, or convergence/divergence) and in the forcings (e.g., bedforms having finite width) introduce 3-D effects. These effects appear minor in the Nordenskiöld case study. The flowline is relatively straight (Figure 6b) and the velocities straddling it are near parallel, including in $210 < x < 370$ km where the major bed topographic features are wide enough to resemble transverse obstacles to flow. We think that these factors, which limit the amount of lateral variations, allow the 2-D flowline approximation to hold well and contribute to the experiment's success. In contrast, 3-D effects probably upset our prediction in the Columbia case study; there we attributed some of the overestimation of undulation amplitude to flow dynamics associated with lateral margins, the underlying valley shape and incoming tributaries (section 3.2). Similar interpretations that shear margins, flow constriction, and 3-D bedforms cause discrepancies in the transfer prediction were made by De Rydt et al. (2013), when they tested the same T_{sb} as used here on ice stream trunks. These authors explained that 2-D transfer functions can overestimate undulation amplitudes because transverse bed perturbations (which render bedforms as 3-D objects) dampen the transmission. Such dampening is predicted by the more general 3-D transfer functions at finite transverse wavelengths (G2003) and confirmed by numerical simulations in 3-D of isothermal quasi-parallel ice flow with basal forcings (Sergienko, 2012).

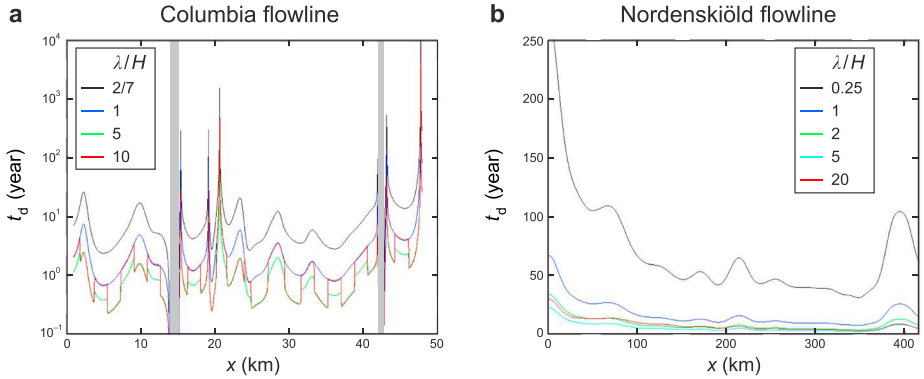

Figure 10. Relaxation time t_d for surface undulations with different wavelengths λ/H along the (a) Columbia flowline and (b) Nordenskiöld flowline (respectively, in logarithmic and linear scales). In each plot, the largest and smallest values of λ/H bracket the mesoscale wavelengths analyzed in our bed-to-surface transmission experiments. In (a), gray bars indicate where vanishing ice surface slope causes $t_d \to \infty$.

Whether the ice flow is steady or evolving matters also. Our method assumes $s(x)$ to have reached steady state and the background to be time invariant. For real flowlines, this adds a further layer of approximation. In the Nordenskiöld case, one might assume that ice flow has not varied substantially for centuries, given the lack of information to the contrary. But Columbia Glacier has been retreating, thinning, and accelerating over recent decades and shows strong seasonal variations in flow speed (section 3.2). Its surface undulations are therefore the lagged response of a transmission that evolves in time. If the glacier-scale change is gradual, however, we may expect to see at different times similar undulations that differ mainly in their details; the seasonal variations should also only perturb $s(x)$ about a mean. Such pseudosteady response may be why s changed negligibly between 2007 and 2012 (Figure 7c). Furthermore, the similarity between the predicted undulations in the experiments forced with spring/autumn speeds and no slip shows that their basic form is insensitive to sliding.

These ideas can be quantified further. For the surface undulations to be pseudosteady, their equilibration or relaxation timescale should be much shorter than the timescale of background evolution. From G2003's equation (72), the relaxation timescale t_d—formally, the e-folding time of the response—is given by

$$t_d = \frac{(1+\gamma)\kappa^3 + P\kappa\cosh\kappa}{\cot\alpha(P\sinh\kappa - \kappa)} \times \frac{[H]}{[u_d]}, \tag{17}$$

where $\kappa = 2\pi/(\lambda/H)$ as before and $[H]$ and $[u_d]$ are the characteristic scales for ice thickness and deformation speed. We estimate t_d using the background values of H and u_d on our flowlines as these scales, so t_d varies not only with wavelength but also with position (Figure 10). For the mesoscale wavelengths studied (the λ/H ranges noted in section 4.1), t_d does not exceed a few decades on the Columbia flowline, except where it reaches very high peaks or infinity, and t_d is $<$100 years on the Nordenskiöld flowline except near the divide. The peaks in t_d are due to high slip ratio and/or low slope (as $t_d \propto (\tan\alpha)(\sin\alpha)^{-n}$); thus, undulations on gently sloping ice flow with enhanced basal slip equilibrate slowly. Figure 10 shows that at each position, t_d decreases with λ/H at short wavelengths and increases with λ/H at long wavelengths to exhibit a minimum, as found by G2003; the shortest undulations ($\lambda/H < 1$) on our flowlines relax most slowly. With the background evolution timescales anticipated above, these results show that pseudosteadiness is met strongly on the Nordenskiöld flowline (especially for $\lambda/H > 1$) and marginally on the Columbia flowline, so $s(x)$ in the latter case is still a valid prediction target for our method.

How well the background and mesoscale variations on a flowline are separated in length scale is another factor determining the method's performance. That the smoothing length L used to extract these components is nonunique reflects our key approximation: each L effectively assumes a different background state for defining the local impulse response. Based on our experience from the case studies, we recommend choosing $L = 10$–$20\bar{H}$. When there is clear separation, the transfer of a mesoscale component with wavelength λ is unaffected if L is varied above λ; and choosing a high L expands the mesoscale wavelength range to be

transferred, without degrading the prediction accuracy much (e.g., Nordenskiöld study). With less separation, L needs to be reduced (e.g., $\lesssim 15\bar{H}$ in the synthetic studies). The Columbia study shows an example where poor scale separation forces us to use $L = 10\bar{H}$ and still leaves behind fast changes on the background and large amplitudes on the perturbations. The maximum prediction accuracy is then rather low (Figure 5b).

In summary, we expect equation (8) to work best for thick ice (which makes the perturbation amplitude relatively small) whose flow has been steady or varying slowly on timescales $\gg t_d$, is not strongly converging/curving/shearing, shows smooth background variations with length scales separated well from the mesoscale perturbations, and occurs over bed topography without major transverse variations (e.g., large longitudinally/diagonally oriented ridges or valleys). These restrictions make the flanks and interiors of ice sheets potentially better places for applying the method than valley/outlet glaciers. The pseudosteadiness requirement may preclude surging glaciers. However, our experiments show that even in adverse cases, the method can mimic the response by capturing the leading-order transmission.

There are also practical issues concerning the inputs. Besides the unknown slipperiness forcing, the bed topography may be inaccurate; the upper half of the Nordenskiöld flowline is a likely example. For cold and polythermal ice masses, the slip ratio γ cannot be reliably estimated without knowledge of their thermal/viscosity structure or measurements of u_d. In the Nordenskiöld study, we inferred $\gamma(x)$ by tuning a thermal correction factor (section 3.3) and those runs are thus not purely predictive. Note that this issue does not arise when numerical modeling is used to follow the thermo-mechanical evolution of the ice mass (section 1), because the simulated coarse grid results naturally include all background variables for our method to be used to predict the mesoscale undulations.

4.4. Further Research

An obvious extension is to generalize the method for time-variable forcings and response in 3-D (perhaps for depth-dependent ice viscosity) by using suitable Fourier transfer functions, some of which had been derived previously (Gudmundsson et al., 1998; G2003). In such effort, it is straightforward to reformulate the convolution in equation (6) as a double integral carrying a 2-D impulse response function. We expect complications from background flow convergence and shearing though. Local coordinate rotation will be needed, as ice flowing in different directions over the bed must yield different responses.

Deriving analytical error estimates/bounds for $s_p(x)$ will facilitate a comprehensive assessment of the factors that hamper our method on real flowlines (even though we have identified the key ones), and this is possible via multiple-scale asymptotic expansion. We foresee obstacles in such derivation. First, the expansion relies on the smallness of a scale-separation parameter (ratio of length scales of short and long variations) but this parameter is not necessarily well defined or easy to determine for real ice flow carrying diverse variations. Second, the first-order problem in the expansion (which, together with the parameter, measures the approximation errors of nonstationary convolution) may not be easy to solve. Third, analytical error bounds for equation (8) cannot be used to predict or evaluate mismatch on flowlines where the complications discussed above operate; deriving error estimates accounting for these is harder still. Meanwhile, it may be fruitful to assess the method's performance and errors statistically by running prediction experiments on many flowlines.

Despite its limitations, our 2-D method can be used to explore 3-D topographic variations on contemporary ice masses, notably ice sheets. By representing their flow with a dense collection of flowlines in plan view, we can begin to study whether the transmission explains the observed mesoscale undulations and how these affect surface water routing (e.g., Ignéczi et al., 2018). For numerically simulated palaeo/future ice sheets, our method can be used to hindcast/predict surface undulations by using their gridded flow variables, circumventing the need for a full Stokes solution. The predictions can inform the calculation of evolving supraglacial water drainage that may feedback on ice sheet dynamics. Important prerequisites for such forward modeling are (i) a reliable subglacial model for describing slipperiness c and (ii) high-resolution bed topographic data (produced nowadays, but still with many gaps).

4.5. Concluding Remarks

The key advance made here is an extension of Gudmundsson's (2003) theory of bed-to-surface transmission for nonuniform ice flow. We derived an approximate yet mathematically consistent model of the transmission and demonstrated its ability to reproduce surface undulations on several synthetic and real flowlines.

While more experiments with the method are needed, it paves the way for a 3-D, time-dependent description. General models of the occurrence of mesoscale undulations on ice should consider the combined effect of the transmission and surface/firn processes and their coupling with mass and energy balance.

Appendix A: Nonuniform Transfer With Wavelets

According to equation (11), the wavelet transform of $s(x)$ is

$$Ws(p,a) = \int_{-\infty}^{\infty} s(x) \frac{1}{\sqrt{a}} \psi^* \left(\frac{x-p}{a} \right) \mathrm{d}x. \tag{A1}$$

Since convolution in the spatial domain is the same as a multiplication operation in the Fourier domain (Convolution theorem), (A1) can be rewritten as

$$Ws(p,a) = \frac{1}{2\pi} \int_{-\infty}^{\infty} \hat{s}(k) \sqrt{a} \hat{\psi}^*(ak) e^{ikp} \, \mathrm{d}k, \tag{A2}$$

where $\hat{\psi}$ is the Fourier transform of the mother wavelet. Now, substituting from equation (7) for $\hat{s}(k)$ predicted by our theory (assuming only topographic transfer, as example) leads to

$$\begin{aligned} Ws(p,a) &= \frac{1}{2\pi} \int_{-\infty}^{\infty} \sqrt{a} \hat{\psi}^*(ak) e^{ikp} \int_{-\infty}^{\infty} T_{\mathrm{sb}}(k,x) b(x) e^{-ikx} \, \mathrm{d}x \, \mathrm{d}k \\ &= \int_{-\infty}^{\infty} b(x) \phi(x,p,a) \, \mathrm{d}x \ , \end{aligned} \tag{A3}$$

where we introduce

$$\phi(x,p,a) = \frac{1}{2\pi} \int_{-\infty}^{\infty} T_{\mathrm{sb}}(k,x) \left[\sqrt{a} \hat{\psi}^*(ak) e^{-ikx} \right] e^{ikp} \, \mathrm{d}k. \tag{A4}$$

Here ϕ represents new wavelets that are the original daughter wavelets filtered by the local properties of T_{sb}. These results show that, to find $s(x)$, one can evaluate the transform integral in (A3) for Ws and take its inverse wavelet transform. However, the nonstationary filtering operation in (A4) implies that the shape of the new wavelets ϕ varies with position, so (A3) is not the standard wavelet transform. Computing (A3) and (A4) involves considerably more work than in our method.

Acknowledgments

We sincerely thank Robert McNabb for providing elevation and velocity data sets and flowline coordinates for Columbia Glacier. We also thank Ian Hewitt and Andrew Fowler for discussions and three reviewers for critical comments. F. S. L. N. acknowledges the support of a William Evans Visiting Fellowship from the University of Otago, New Zealand and the support of a UK Leverhulme Trust Research Fellowship (RF-2017-320). A. I. acknowledges PhD funding from the Ice and Climate Research at Sheffield group; S. J. L. and A. J. S. acknowledge a White Rose Universities Consortium Collaboration Grant. The input and output data of our experiments, as well as MATLAB code for computing the nonuniform transfer, are archived in the University of Sheffield's Online Research Data (ORDA) Repository at https://doi.org/10.15131/shef.data.6014072.v1.

References

Alessio, S. (2016). *Digital signal processing and spectral analysis for scientists*. Cham, Switzerland: Springer. https://doi.org/10.1007/978-3-319-25468-5

Arnold, N. S., Gareth Rees, W., Hodson, A. J., & Kohler, J. (2006). Topographic controls on the surface energy balance of a high Arctic valley glacier. *Journal of Geophysical Research*, *111*, F02011. https://doi.org/10.1029/2005JF000426

Black, H. P., & Budd, W. (1964). Accumulation in the region of Wilkes, Wilkes Land, Antarctica. *Journal of Glaciology*, *5*(37), 3–15. https://doi.org/10.1017/S0022143000028549

Budd, W. F. (1970). Ice flow over bedrock perturbations. *Journal of Glaciology*, *9*(55), 29–48. https://doi.org/10.1017/S0022143000026770

Cuffey, K. M., & Paterson, W. S. B. (2010). *The physics of glaciers* (4th ed.). New York: Academic Press.

De Rydt, J., Gudmundsson, G. H., Corr, H. F. J., & Christoffersen, P. (2013). Surface undulations of Antarctic ice streams tightly controlled by bedrock topography. *The Cryosphere*, *7*(2), 407–417. https://doi.org/10.5194/tc-7-407-2013

Fahnestock, M., Scambos, T. A., Moon, T., Gardner, A. S., Haran, T., & Klinger, M. (2016). Rapid large area mapping of ice flow using Landsat 8. *Remote Sensing of Environment*, *185*, 84–94. https://doi.org/10.1016/j.rse.2015.11.023

Fahnestock, M. A., Scambos, T. A., Shuman, C. A., Arthern, R. J., Winebrenner, D. P., & Kwok, R. (2000). Snow megadune fields on the East Antarctic plateau: Extreme atmosphere-ice interactions. *Geophysical Research Letters*, *27*(22), 3719–3722. https://doi.org/10.1029/1999GL011248

Frezzotti, M., Urbini, S., Proposito, M., Scarchilli, C., & Gandolfi, S. (2007). Spatial and temporal variability of surface mass balance near Talos dome, East Antarctica. *Journal of Geophysical Research*, *112*, F02032. https://doi.org/10.1029/2006JF000638

Gow, A. J., & Rowland, R. (1965). On the relationship of snow accumulation to surface topography at "Byrd Station", Antarctica. *Journal of Glaciology*, *5*(42), 843–847. https://doi.org/10.1017/S0022143000018906

Gudmundsson, G. H. (2003). Transmission of basal variability to a glacier surface. *Journal of Geophysical Research*, *108*(B5), 2253. https://doi.org/10.1029/2002JB002107

Gudmundsson, G. H., Raymond, C. F., & Bindschadler, R. (1998). The origin and longevity of flow stripes on Antarctic ice streams. *Annals of Glaciology*, *27*, 145–152. https://doi.org/10.3189/1998AoG27-1-145-152

Harrington, J. A., Humphrey, N. F., & Harper, J. T. (2015). Temperature distribution and thermal anomalies along a flowline of the Greenland ice sheet. *Annals of Glaciology*, *56*(70), 98–104. https://doi.org/10.3189/2015AoG70A945

Howat, I., Negrete, A., & Smith, B. (2014). The Greenland Ice Mapping Project (GIMP) land classification and surface elevation data sets. *The Cryosphere*, *8*(4), 1509–1518. https://doi.org/10.5194/tc-8-1509-2014

Howat, I., Negrete, A., & Smith, B. (2017). *MEaSUREs Greenland Ice Mapping Project (GIMP) digital elevation model from GeoEye and WorldView imagery, version 1*. Boulder, CO: NASA National Snow and Ice Data Center Distributed Active Archive Center. https://doi.org/10.5067/H0KUYVF53Q8M

Ignéczi, A., Sole, A. J., Livingstone, S. J., Leeson, A. A., Fettweis, X., Selmes, N., et al. (2016). Northeast sector of the Greenland ice sheet to undergo the greatest inland expansion of supraglacial lakes during the 21st century. *Geophysical Research Letters*, *43*, 9729–9738. https://doi.org/10.1002/2016GL070338

Ignéczi, A., Sole, A. J., Livingstone, S. J., Ng, F. S. L., & Yang, K. (2018). Greenland Ice Sheet surface topography and drainage structure controlled by the transfer of basal variability. *Frontiers in Earth Science: Cryospheric Sciences*, *6*, 101. https://doi.org/10.3389/feart.2018.00101

Jóhannesson, T. (1992). Landscape of temperate ice caps, (PhD thesis). University of Washington, Seattle.

Joughin, I., Das, S. B., Flowers, G. E., Behn, M. D., Alley, R. B., King, M. A., et al. (2013). Influence of ice-sheet geometry and supraglacial lakes on seasonal ice-flow variability. *The Cryosphere*, *7*(4), 1185–1192. https://doi.org/10.5194/tc-7-1185-2013

Joughin, I., Smith, B., Howat, I. M., Scambos, T., & Moon, T. (2010). Greenland flow variability from ice-sheet-wide velocity mapping. *Journal of Glaciology*, *56*(197), 415–430. https://doi.org/10.3189/002214310792447734

Karlstrom, L., & Yang, K. (2016). Fluvial supraglacial landscape evolution on the Greenland ice sheet. *Geophysical Research Letters*, *43*, 2683–2692. https://doi.org/10.1002/2016GL067697

Kevorkian, J. K., & Cole, J. D. (1996). *Multiple scale and singular perturbation methods*. New York: Springer.

Korona, J., Berthier, E., Bernard, M., Rémy, F., & Thouvenot, E. (2009). SPIRIT. SPOT 5 stereoscopic survey of polar ice: Reference images and topographies during the fourth international polar year (2007–2009). *ISPRS Journal of Photogrammetry and Remote Sensing*, *64*(2), 204–212. https://doi.org/10.1016/j.isprsjprs.2008.10.005

Lampkin, D. J., & VanderBerg, J. (2011). A preliminary investigation of the influence of basal and surface topography on supraglacial lake distribution near JakobshavnIsbrae, western Greenland. *Hydrological Processes*, *25*(21), 3347–3355. https://doi.org/10.1002/hyp.8170

MacAyeal, D. R. (1993). A tutorial on the use of control methods in ice-sheet modelling. *Journal of Glaciology*, *39*(131), 91–98. https://doi.org/10.1017/S0022143000015744

MacGregor, J. A., Fahnestock, M. A., Catania, G. A., Aschwanden, A., Clow, G. D., Colgan, W. T., et al. (2016). A synthesis of the basal thermal state of the Greenland ice sheet. *Journal of Geophysical Research: Earth Surface*, *121*, 1328–1350. https://doi.org/10.1002/2015JF003803

Mallat, S. (2009). *A wavelet tour of signal processing: The sparse way* (3rd ed.). Burlington, USA: Academic Press.

Margrave, G. F. (1998). Theory of nonstationary linear filtering in the Fourier domain with application to time-variant filtering. *Geophysics*, *63*(1), 244–259. https://doi.org/10.1190/1.1444318

McNabb, R. W., Hock, R., O'Neel, S., Rasmussen, L. A., Ahn, Y., Braun, M., et al. (2012). Using surface velocities to calculate ice thickness and bed topography: A case study at Columbia Glacier, Alaska, USA. *Journal of Glaciology*, *58*(212), 1151–1164. https://doi.org/10.3189/2012JoG11J249

Medley, B., Ligtenberg, S. R. M., Joughin, I., Van den Broeke, M. R., Gogineni, S., & Nowicki, S. (2015). Antarctic firn compaction rates from repeat-track airborne radar data: I. Methods. *Annals of Glaciology*, *56*(70), 155–166. https://doi.org/10.3189/2015AoG70A203

Meier, M. F., Rasmussen, L. A., Krimmel, R. M., Olsen, R. W., & Frank, D. (1985). Photogrammetric determination of surface altitude, terminus position, and ice velocity of Columbia Glacier, Alaska. *USGS Professional Paper*, *1258-F*, 29–38.

Meierbachtol, T. W., Harper, J. T., Johnson, J. V., Humphrey, N. F., & Brinkerhoff, D. J. (2015). Thermal boundary conditions on western Greenland: Observational constraints and impacts on the modeled thermomechanical state. *Journal of Geophysical Research: Earth Surface*, *120*, 623–636. https://doi.org/10.1002/2014JF003375

Morlighem, M., Rignot, E., Mouginot, J., Seroussi, H., & Larour, E. (2014). Deeply incised submarine glacial valleys beneath the Greenland ice sheet. *Nature Geoscience*, *7*(6), 418–422. https://doi.org/10.1038/ngeo2167

Morlighem, M., Rignot, E., Mouginot, J., Seroussi, H., & Larour, E. (2015). *IceBridge BedMachine Greenland, version 2*. Boulder, CO: NASA DAAC at the National Snow and Ice Data Center. https://doi.org/10.5067/AD7B0HQNSJ29

Murray, T., Dowdeswell, J. A., Drewry, D. J., & Frearson, I. (1998). Geometric evolution and ice dynamics during a surge of Bakaninbreen, Svalbard. *Journal of Glaciology*, *44*(147), 263–272. https://doi.org/10.1017/S0022143000002604

O'Neel, S., Pfeffer, W. T., Krimmel, R., & Meier, M. (2005). Evolving force balance at Columbia Glacier, Alaska, during its rapid retreat. *Journal of Geophysical Research*, *110*, F03012. https://doi.org/10.1029/2005JF000292

Price, S. F., Hoffman, M. J., Bonin, J. A., Howat, I. M., Neumann, T., Saba, J., et al. (2017). An ice sheet model validation framework for the Greenland ice sheet. *Geoscientific Model Development*, *10*(1), 255–270. https://doi.org/10.5194/gmd-10-255-2017

Raymond, M. J., & Gudmundsson, G. H. (2005). On the relationship between surface and basal properties on glaciers, ice sheets, and ice streams. *Journal of Geophysical Research*, *110*, B08411. https://doi.org/10.1029/2005JB003681

Reeh, N. (1987). Steady-state three-dimensional ice flow over an undulating base: First-order theory with linear ice rheology. *Journal of Glaciology*, *330*, 177–185.

Sergienko, O. V. (2012). The effects of transverse bed topography variations in ice-flow models. *Journal of Geophysical Research*, *117*, F03011. https://doi.org/10.1029/2011JF002203

Sergienko, O. V., & Hindmarsh, R. C. A. (2013). Regular patterns in frictional resistance of ice-stream beds seen by surface data inversion. *Science*, *342*(6162), 1086–1089. https://doi.org/10.1126/science.1243903

Vijay, S., & Braun, M. (2017). Seasonal and interannual variability of Columbia Glacier, Alaska (2011–2016): Ice velocity, mass flux, surface elevation and front position. *Remote Sensing*, *9*(6), 635. https://doi.org/10.3390/rs9060635

Whillans, I. M. (1975). Effect of inversion winds on topographic detail and mass balance on inland ice sheets. *Journal of Glaciology*, *14*(70), 85–90. https://doi.org/10.1017/S0022143000013423

Wyatt, F. R., & Sharp, M. J. (2015). Linking surface hydrology to flow regimes and patterns of velocity variability on Devon ice cap, Nunavut. *Journal of Glaciology*, *61*(226), 387–399. https://doi.org/10.3189/2015JoG14J109